Eliminate Crosstalk Using Symmetry in MIMO Arrays of Inductive Antennas: The Pie-Chart Antennas

Jean-Philippe Douarville-Blaise

Thesis directors: *Junji Hirai, Satoshi Komada*

A thesis presented for the degree of

Doctor of Philosophy

Division of System Engineering

Mie University, Japan

September 2017

Eliminate Crosstalk Using Symmetry in MIMO Arrays of Inductive Antennas: The Pie-Chart Antennas

Jean-Philippe Douarville-Blaise[1]

Thesis directors: *Junji Hirai, Satoshi Komada*

Abstract

Whoever ever had a conversation in the middle of a noisy room can understand how badly crosstalk can affect a communication system. Crosstalk is a form of noise. It is a major concern in electronic design. Indeed, as our communication systems grow in size and complexity, so does the crosstalk suppression issue. And with it, the complexity and/or the price of the solutions. Through this thesis, I would like to present you my piece of solution to effectively reduce crosstalk at low cost within multichannel transmission systems.

The Pie-Chart antenna concept is a simple yet effective method of designing arrays of antennas so that emitters and receivers can communicate through highly independent transmission channels. In a nutshell, a Pie-Chart channel (or pie channel) is defined by its order of symmetry around a longitudinal axis, thus describing an axis-symmetric azimuthal emission/reception diversity pattern. A different order of symmetry around the same axis defines a physically different channel. Every pie arrays of the same order of symmetry around this axis can communicate with each other. While transmissions from arrays of a different order are heavily rejected through a passive form of destructive interference noise cancellation. This concept is expendable past the limited frame of electromagnetism (acoustic, vibrations and wave-signals in general) and its applicability goes beyond the sole field of wireless transmission.

However very intuitive to understand and apparently fruitful in term of its applicability, the result of preliminary state-of-the-art researches revealed that this concept have

[1]Contact: pier.jp.douarvil@gmail.com

seemingly not already been reported up to present (too trivial to be treated?). Therefore, within the course of this PhD. I developed an electromagnetic model describing the theoretical operation of the presented concept. I set and realized several experiments which results show good agreement with the model's predictions. I discussed how could exiting devices benefit from the proposed solution. And finally, I conceptualized new applications made possible by the Pie-Chart antenna concept. Through the hereby manuscript, I will present you a synthesis of this journey and its major outcomes.

This thesis is my modest contribution to the accretion and the transmission of mankind knowledges. As a matter of fact, it is written so that to be understandable by anyone having knowledges in euclidean geometry, basis in electricity, linear algebra as well as differential and integral calculus. May this humble piece of work be wisely used to your fulfillment.

A Glance At...

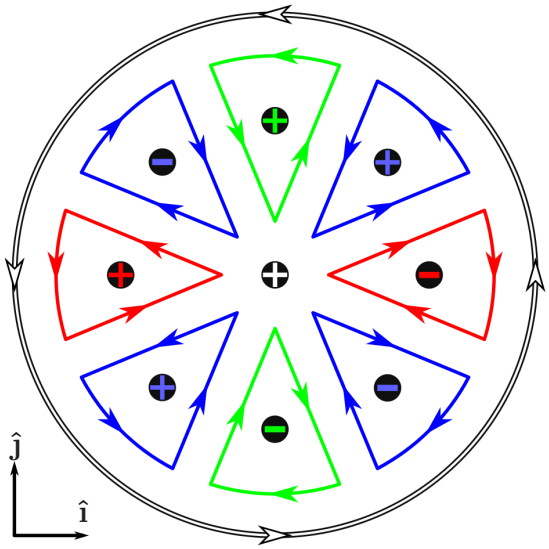

Figure 1: This figure can be seen as the conductor layout of a flat (e.g. tracks of a PCB) 4 channels Pie-Chart inductive emitter (or receiver). Red and green oriented paths would respectively represent the 2^{nd} and 3^{rd} channels emitter's (receiver's) track. They both are 2^{nd} order Pie-Chart arrays. Blue oriented path would represent the 4^{th} channel emitter's (receiver's) track. It is a 3^{rd} order Pie-Chart array. White oriented outer circle would represent the 1^{st} channel emitter's (receiver's) track. It is a special 1^{st} order Pie-Chart antenna: it has infinite number of plane of anti-symmetry. Plus and minus signs indicate the magnetic field's orientation along the $\widehat{\mathbf{k}}$ axis given the correspondingly colored current paths.

This figure can also be seen as the cross-section of a 4 channels Pie-Chart cable, or that of 4 channels Pie-Chart non-contact linear sliding connection: plus and minus signs would then indicate the location of the conductors and the orientation of their current along the $\widehat{\mathbf{k}}$ axis while the colored oriented paths would indicate the corresponding magnetic field's orientation. In the case of a cable however, the 1^{st} channel is incomplete (only one wire represented by the white plus sign). A concentric cylindrical conductive sleeve braided around the whole cable would provide an ideal return line for this channel as it will also provide additional shielding to the cable. In other word, it may represent the cross section of a true form of 4 channels coaxial cable!

Dedication

To mankind:

May this humble piece of work be wisely used to your fulfillment.

To my friends:

Without whom I wouldn't have, ever, gone so far.

To my parents:

May this manuscript make you proud of your genes, your education, your sacrifices, of me. YOU are my heros.

To my lover:

Without whom I don't picture the future.

Declaration

I certify that this work contains no material which has been accepted for the award of a degree or diploma in my name by a University or any other institution and, to the best of my knowledge and belief, contains no material previously published or written by another person, except by the way of background information and references duly acknowledge in the text. However this manuscript may include parts of scientific journal articles originally written by me for the purpose of this PhD course.

Date: _____ Sign: _____

Acknowledgement

This research was financially supported by the Department of Education of the “Collectivité Territoriale de Martinique”.

Symbols and Abbreviations

Abbreviation	**Meaning**	**Unit**
$TAWT$	Transverse Axis Wind Turbine	NA
μ	vacuum permeability	H/m
ϵ	vacuum permittivity	F/m
$\vec{H}$	Magnetic field	A/m
$\vec{B}$	Magnetic flux density	T
$\vec{E}$	Electric field	N/C
$\vec{D}$	Electric flux density	C/m^2
$\vec{i}$	Electric current	A
$\vec{J}$	Electric current density	A/m^2
R	electric resistance	Ω
ESR	**E**quivalent **S**erial **R**esistance	Ω

Contents

Chapter 1

Introduction

BEWARE: uninitiated readers who got intimidated by the long title, some specific terms in the abstract, or this unexpected BEWARE statement, might be shocked at how easy to understand is the Pie-Chart antenna concept. To them, I will remind this idiom:

> "*One should not judge a book by its cover.*"

1.1 Context

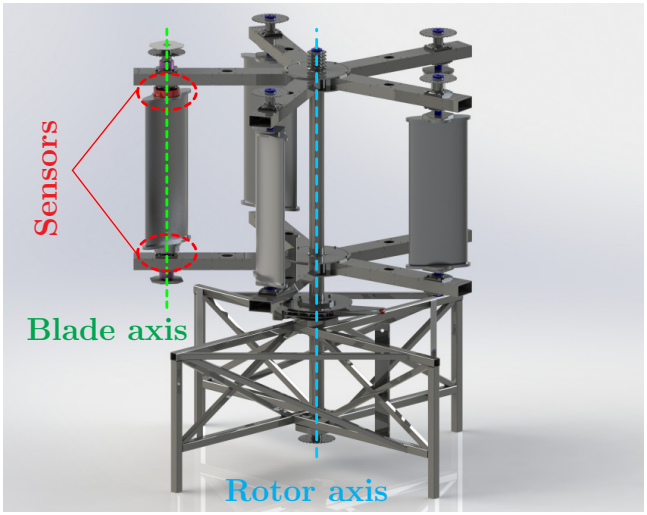

Figure 1.1: CAD view of a highly reconfigurable Wollongong VAWT prototype.

This PhD research project was initially intended at characterizing and improving

the performance of the so called Wollongong Transverse Axis Wind Turbine (TAWT). As you can see on the Fig. 1.1, the blades of a Wollongong TAWT rotates about an axis, which one is orbiting around the rotor's central axis. The Pie-Chart antenna concept arose from a very practical concern: how to monitor in real-time the output of the transducers placed on a moving blade from a stationary platform. This problem is commonly addressed using batteries, slip rings and/or widespread wireless technologies such as W-LAN, Bluetooth, ZigBee, etc. [1–4].

Slip rings are very popular for transmitting high power or multiple signal in a small package. However, not only they are subject to the same electromagnetic design challenges as non-contact Multiple-Inputs Multiple-Outputs (MIMO) devices at high frequency (e.g. electrical path length, impedance matching, crosstalk) but they also require periodic servicing due to mechanical wear [5]. On the other hand, wireless data transmission protocols such as Bluetooth or W-LAN are currently not suited for wireless transmission of substantial electric power. As a result, Near-Field Wireless Transmission of Power and Information technologies (NFWTPI) are increasingly considered as a viable alternative solution: more than 80000 patents were filled in 2014 [6] on the theme of "*Wireless power transmission*".

1.2 About Crosstalk

Imagine you listening to a friend in a quiet room (Fig. 1.2). You, the receiver, and your friend, the emitter, are forming a conversation channel. Now add 2 more speakers, speaking to 2 other listeners in this same room. They form 2 different conversation channels. Yet, because you are all in the same room, every listener can hear more or less every speaker. This is crosstalk. And, if the speakers are all close together, speak with similar tone, speed and volume as your friend do, you may find it difficult or even impossible to follow your own friend's speech. In summary, crosstalk is a form of signal disturbance, of noise, which is due to the leakage of energy from an "agressor" transmission system into a "victim". It may affect sound speakers and microphones, capacitive antennas, inductive antennas or more generally electromagnetic devices. This disturbance may result in a mere increase of Bit Error Rate (BER) to a complete communication disruption or even cause hardware damages. For example it is one of the first limit to the maximum length, operating frequency or number of channels of Ethernet cables.

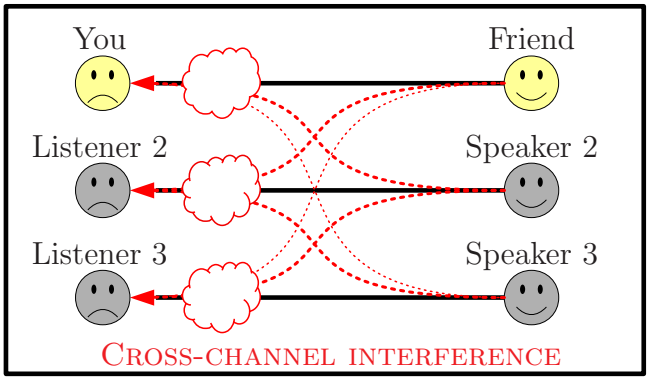

Figure 1.2: Basic illustration of crosstalk disturbance.

1.3 Stakes and Solutions

What if we could increase data rate while reducing bit error rate, development time and production cost of wired and wireless signal transmissions systems? In this manuscript we present our contribution to those concerns in the form of a simple concept: the Pie-Chart antenna.

Crosstalk is a challenging issue for compact high data rate MIMO NFWTPI devices. Given the current limitations of semi-conductor based solid-state electrical components [7], the higher the handled electric power the lower must be its carrier frequency. Therefore high power compact NFWTPI devices commonly rely on a low frequency power supply channel separated from a high frequency data channel. Crosstalk is then mitigated using a combination of high cross-channel reluctance(shielding included), electronic filters, or other exotic active solutions [8–11] thus limiting the systems simplicity, compactness, weight or reliability.

In his paper [12], T. Bieler proposes a very simple and compact crosstalk cancellation solution: power and information are transmitted by induction on two physically distinct channels. Each channel consists in a coil of specific geometry organized so that the mutual inductance between two different channels is reduced to the minimum. The beauty of his solution lies in that, however the power coil is almost wound into the data coil, crosstalk is very low. When dealing with high power antennas in near-field to data transmission systems, such a solution can significantly reduce the need for magnetic guides, shielding or electronic components [20], hence potentially lowering weight, size, complexity, cost and increasing reliability of transmission systems. The Pie-Chart antenna concept is an extension of T. Bieler's solution to higher number of channels. In

it most basic expression, it can be assimilated as a form of mutual inductance cancellation using symmetries. What makes it interesting is its simplicity and its capacity to suppress crosstalk among a theoretically infinite number of channels.

In this thesis, we describe the theory behind this concept, a wide variety of potential applications, from telecommunication to metrology, and the limits of the concept. We extensively illustrate crosstalk suppression's effectiveness of the different Pie-Charts antennas models through the results of numerical and real experiments detailed in this manuscript. Its content is presented as an enriched compilation of researches published in the context of this PhD.

Chapter 2

Pie-chart Basics

2.1 Prerequisite

In the following we consider a working medium of linear homogeneous isotropic electromagnetic properties filling an infinite tridimensional euclidean space. The medium has a magnetic permeability $\mu = \mu_0\mu_r$ and relative permittivity $\varepsilon = \varepsilon_0\varepsilon_r$, where μ_r is its relative permeability, ε_r its relative permittivity, $\mu_0 = 4\pi \times 10^7\,\mathrm{T\,m\,A^{-1}}$ and $\varepsilon_0 = {\mu_0}^{-1}c^{-2}\mathrm{F\,m^{-1}}$. The default Cartesian frame of reference is defined as $(O;\hat{\mathbf{i}},\hat{\mathbf{j}},\hat{\mathbf{k}})$.

2.1.1 Definitions

Reflexive Symmetry Function

Suppose a plane $Q_{\vec{n},\vec{A}}$ normal to a vector $\vec{n} = n_x\hat{\mathbf{i}} + n_y\hat{\mathbf{j}} + n_z\hat{\mathbf{k}} \neq \vec{0}$ and including a point A located by $\vec{A} = \overrightarrow{OA} = A_x\hat{\mathbf{i}} + A_y\hat{\mathbf{j}} + A_z\hat{\mathbf{k}}$. The function $Z(\vec{P},\vec{n},\vec{A})$ which associates to any point P its orthogonal symmetric $\underset{\vec{n},\vec{A}}{\widetilde{P}}$ by the plane $Q_{\vec{n},\vec{A}}$ (Fig. 2.1) is defined by:

$$\begin{array}{rcl} Z : (\mathbb{R}^3,\mathbb{R}^3,\mathbb{R}^3) & \rightarrow & \mathbb{R}^3 \\ (\vec{P},\vec{n},\vec{A}) & \mapsto & \widetilde{P} = \dfrac{1}{\vec{n}^2}\left(2\,[\mathbf{B}]\,\vec{A} + [\mathbf{C}]\,\vec{P}\right) \end{array} \tag{2.1}$$

where $[\mathbf{B}] = \vec{n}^T \times \vec{n}$ ($\vec{n}$ is a row vector) and $[\mathbf{C}] = \vec{n}^2 \times [\mathbf{I}]_3 - 2\,[\mathbf{B}]$ ($[\mathbf{I}]_3$ is the 3×3 unit matrix). Then:

- Z is an isometry of the euclidean space.

- For any given vectors $\vec{U}$ and $\vec{V}$:

$$\overset{\vec{n},\vec{A}}{\widetilde{U}} - \overset{\vec{n},\vec{A}}{\widetilde{V}} = \overbrace{\vec{U} - \vec{V}}^{\vec{n},\vec{A}} \tag{2.2}$$

$$\overset{\vec{n},\vec{0}}{\widetilde{U}} \times \overset{\vec{n},\vec{0}}{\widetilde{V}} = -\overbrace{\vec{U} \times \vec{V}}^{\vec{n},\vec{0}} \tag{2.3}$$

$$\overset{\vec{n},\vec{0}}{\widetilde{U}} \cdot \overset{\vec{n},\vec{0}}{\widetilde{V}} = \vec{U} \cdot \vec{V} \tag{2.4}$$

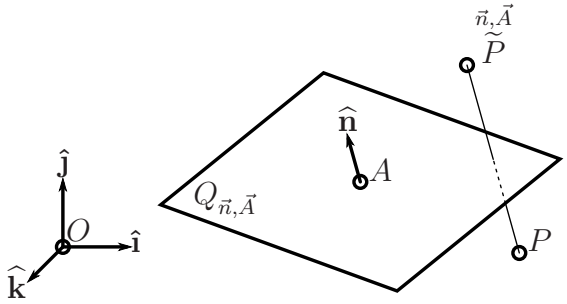

Figure 2.1: $\overset{\vec{n},\vec{A}}{\widetilde{P}}$ symmetric of P through $Q_{\vec{n},\vec{A}}$.

Antenna

The term antenna refers to any closed oriented 3D path. We model it as a parametric curve:

$$\begin{array}{rcl} \zeta :]a,b[& \to & \mathbb{R}^3 \\ t & \mapsto & \vec{\zeta}(t) = \begin{pmatrix} x(t) \\ y(t) \\ z(t) \end{pmatrix}_{\widehat{\mathbf{i}},\widehat{\mathbf{j}},\widehat{\mathbf{k}}} \end{array} \tag{2.5}$$

differentiable on $]a,b[$ where $\lim_{t\to a} \vec{\zeta}(t) = \lim_{t\to b} \vec{\zeta}(t)$ are respectively the positive and negative antenna's terminals.

The electric current $\vec{i}(t)$ through ζ is defined at each point $\vec{\zeta}(t)$ by:

$$\vec{i}(t) = i(t) \cdot \frac{\vec{\zeta}'(t)}{\|\vec{\zeta}'(t)\|} \tag{2.6}$$

where $i(t) \in \mathbb{R}$ is the current intensity and $\vec{\zeta}'(t) \,/\, \|\vec{\zeta}'(t)\|$ is the curve's orientation vector at $\vec{\zeta}(t)$.

Array

An array [of antennas] refers to a tuple of n antennas $\vec{\zeta_i}$, where $n \in \mathbb{N}$, all linked to a common signal S via transfer functions of their electric current $\vec{i_i}(t, S)$ or electric potential $V_i(t, S)$ at each point $\vec{\zeta_i}(t)$.

Magneto-static Approximation

In this paper, we consider that, at any instant, the current's wavelength is long enough to be consider of uniform intensity along each individual filamentary antenna it flows in. Therefore the mutual inductance $M_{i,j}$ between two antennas ζ_i and ζ_j can be determined using the following Neumann Equation [13]:

$$M_{i,j} = \frac{\mu}{4\pi} \cdot \oint_{\zeta_i} \oint_{\zeta_j} \frac{\vec{dl}_i \cdot \vec{dl}_j}{\|\vec{r}_{i,j}\|} \tag{2.7}$$

where $\vec{dl}_i = \vec{\zeta}'_i(t_i)\, dt_i$, $\vec{dl}_j = \vec{\zeta}'_j(t_j)\, dt_j$ and $\vec{r}_{i,j} = \vec{\zeta}_j(t_j) - \vec{\zeta}_i(t_i)$. Given that $\vec{dl}_i$ and $\vec{dl}_j$ are independent, this equation leads to $M_{i,j} = M_{j,i}$.

2.1.2 Mutual inductance cancellation

In this subsection the parameters $\vec{n}$ and $\vec{A}$ are constants. Readers may refer to Fig. 2.2 of the Subsection 2.1.2 for visual reference.

Emitters Geometry

ζ_E is an emitting array of m geometrically distinct antennas such as $Q_{\vec{n},\vec{A}}$ is a plane of anti-symmetry of ζ_E (symmetric paths but reverse symmetric orientation). That is to say, the elements ζ_{E_i} of ζ_E are constrained in shape and orientation in the manner:

$$\forall i \leq m, i \in \mathbb{N}^* \ : \ \exists! j / \zeta_{E_i} :$$

$$\begin{array}{rcl}]-e, e[& \to & \mathbb{R}^3 \\ \alpha & \mapsto & \left| \begin{array}{rcl} \vec{\zeta}_{E_i}(\alpha) & = & \overset{\vec{n},\vec{A}}{\widetilde{\zeta}}_{E_j}(-\alpha) \\ \vec{\zeta}'_{E_i}(\alpha) & = & -\overset{\vec{n},\vec{0}}{\widetilde{\zeta}}'_{E_j}(-\alpha) \end{array} \right. \end{array} \tag{2.8}$$

For conciseness, we will use the notation $\zeta_{E_i} = \overset{\vec{n},\vec{A}}{\rightleftharpoons} \zeta_{E_j}$ to represent this relation of reflexive *anti-symmetry* by the plane $Q_{\vec{n},\vec{A}}$ between the two individual antennas ζ_{E_i} and ζ_{E_j}. By extension, we will use this same notation $\zeta_E = \overset{\vec{n},\vec{A}}{\rightleftharpoons} \zeta_E$ to represent the reflexive anti-symmetry relation between two arrays ζ_E and $\overset{\vec{n},\vec{A}}{\rightleftharpoons} \zeta_E$.

ζ_F is an emitting antenna array of n geometrically distinct antennas such as $Q_{\vec{n},\vec{A}}$ is a plane of symmetry of ζ_F. That is to say, the elements ζ_{F_i} of ζ_F are constrained in shape and orientation in the manner:

$$\forall i \leq n, i \in \mathbb{N}^* \ : \ \exists! j / \ \ \zeta_{F_i} :$$

$$\begin{array}{rcl}]-f,f[& \rightarrow & \mathbb{R}^3 \\ \alpha & \mapsto & \left| \begin{array}{rcl} \vec{\zeta}_{F_i}(\alpha) & = & \overset{\vec{n},\vec{A}}{\sim} \zeta_{F_j}(\alpha) \\ \vec{\zeta\prime}_{F_i}(\alpha) & = & \overset{\vec{n},\vec{0}}{\sim} \zeta\prime_{F_j}(\alpha) \end{array} \right. \end{array} \tag{2.9}$$

For conciseness, we will use the notation $\zeta_{F_i} = \overset{\vec{n},\vec{A}}{\leftleftharpoons} \zeta_{F_j}$ to represent this relation of reflexive symmetry by the plane $Q_{\vec{n},\vec{A}}$ between the two individual antennas ζ_{F_i} and ζ_{F_j}. By extension, we will use this same notation $\zeta_F = \overset{\vec{n},\vec{A}}{\leftleftharpoons} \zeta_F$ to represent the reflexive symmetry relation between two arrays ζ_F and $\overset{\vec{n},\vec{A}}{\leftleftharpoons} \zeta_F$.

Receivers Geometry

ζ_G and ζ_H are receiving arrays of respectively o and p geometrically distinct antennas defined on $]-g,g[$ and $]-h,h[$ such as:

$$\zeta_G = \overset{\vec{n},\vec{A}}{\rightleftharpoons} \zeta_G \tag{2.10}$$

$$\zeta_H = \overset{\vec{n},\vec{A}}{\leftleftharpoons} \zeta_H \tag{2.11}$$

Mutual Inductance

Considering the above described antenna configuration, we can determined the mutual inductance between each couple of antennas of ζ_E and ζ_F as:

$$\begin{aligned}
&\forall (i,k) \leq (m,n), (i,k) \in \mathbb{N}^{2*} : \\
&\qquad M_{E_i,F_k} \\
&\qquad = \frac{\mu}{4\pi} \cdot \int_{-e}^{e} \int_{-f}^{f} \frac{- \overset{\vec{n},\vec{A}}{\widetilde{\zeta}'_{E_j}}(-\alpha) \cdot \overset{\vec{n},\vec{A}}{\widetilde{\zeta}'_{F_l}}(\beta)}{\| \overset{\vec{n},\vec{A}}{\widetilde{\zeta}_{F_l}}(\beta) - \overset{\vec{n},\vec{A}}{\widetilde{\zeta}_{E_j}}(-\alpha) \|} \, d\beta \, d\alpha \\
&\qquad = \frac{\mu}{4\pi} \cdot \int_{-e}^{e} \int_{f}^{-f} \frac{- \overset{\vec{n},\vec{A}}{\widetilde{\zeta}'_{E_j}}(\gamma) \cdot \overset{\vec{n},\vec{A}}{\widetilde{\zeta}'_{F_l}}(\beta)}{\| \overset{\vec{n},\vec{A}}{\widetilde{\zeta}_{F_l}}(\beta) - \overset{\vec{n},\vec{A}}{\widetilde{\zeta}_{E_j}}(\gamma) \|} \, d\gamma \, d\beta \\
&\qquad = - M_{E_j,F_l}
\end{aligned} \tag{2.12}$$

where $\zeta_{E_i} = \overset{\vec{n},\vec{A}}{\rightleftharpoons}{\zeta}_{E_j}$ and $\zeta_{F_k} = \overset{\vec{n},\vec{A}}{\Leftarrow}{\zeta}_{F_l}$. Similarly, we can establish that:

$(i,k) \in \mathbb{N}^{2*}$:

$$\forall (i,k) \leq (m,o) \ : \ M_{E_i,G_k} = M_{E_j,G_l} \tag{2.13}$$

$$\forall (i,k) \leq (m,p) \ : \ M_{E_i,H_k} = -M_{E_j,H_l} \tag{2.14}$$

$$\forall (i,k) \leq (n,o) \ : \ M_{F_i,G_k} = -M_{F_j,G_l} \tag{2.15}$$

$$\forall (i,k) \leq (n,p) \ : \ M_{F_i,H_k} = M_{F_j,H_l} \tag{2.16}$$

$$\forall (i,k) \leq (o,p) \ : \ M_{G_i,H_k} = -M_{G_j,H_l} \tag{2.17}$$

$i \in \mathbb{N}^*$:

$$\forall i \leq m \ : \ M_{E_i,E_i} = M_{E_j,E_j} \tag{2.18}$$

$$\forall i \leq n \ : \ M_{F_i,F_i} = M_{F_j,F_j} \tag{2.19}$$

$$\forall i \leq o \ : \ M_{G_i,G_i} = M_{G_j,G_j} \tag{2.20}$$

$$\forall i \leq p \ : \ M_{H_i,H_i} = M_{H_j,H_j} \tag{2.21}$$

where $\zeta_{G_i} = \overset{\vec{n},\vec{A}}{\rightleftharpoons}{\zeta}_{G_j}$ and $\zeta_{H_k} = \overset{\vec{n},\vec{A}}{\Leftarrow}{\zeta}_{H_l}$.

Given the above relations, the fact that the EMF ΔV_i across the terminals of an inductor ζ_i induced by the current of uniform intensity i_j flowing through an antenna

ζ_j can be determined at any instant t using Faraday's law as follow

$$\Delta V_i = M_{ij} \frac{d\ i_j}{dt} \tag{2.22}$$

and reminding that every antenna's current or electromotive force (EMF) of a given array are linked to one common signal via transfer functions (cf. Section 2.1.1), one can think of ways to combine the antennas so that the output signal $S_G(t)$ of ζ_G depends only on the input signal $S_E(t)$ of ζ_E and the output signal $S_H(t)$ of ζ_H only on the input signal $S_F(t)$ of ζ_F. In the following subsection, we present the simplest antenna combination which meets those requirements.

Mutual Inductance Compensation Layout

We combine each emitting antenna ζ_{E_i} of ζ_E with its anti-symmetric ζ_{E_j} such as at each instant t :

$\forall i \in \mathbb{N}^*, i \leq m$:

$$\zeta_{E_i} \cup \zeta_{E_j} \Leftrightarrow \frac{di_{E_i}}{dt} = \frac{di_{E_j}}{dt} = \mathcal{F}_{E_i}(S_E(t)) \tag{2.23}$$

where $\mathcal{F}_{E_i}$ is an arbitrary transfer function. Similarly, we combine each emitting antenna ζ_{F_i} of ζ_F with its symmetric ζ_{F_j} such as at each instant t :

$\forall i \in \mathbb{N}^*, i \leq n$:

$$\zeta_{F_i} \cup \zeta_{F_j} \Leftrightarrow \frac{d\ i_{F_i}}{dt} = \frac{d\ i_{F_j}}{dt} = \mathcal{F}_{F_i}(S_F(t)) \tag{2.24}$$

where $\mathcal{F}_{F_i}$ is an arbitrary transfer function.

We now combine each receiving antennas ζ_{G_i} of ζ_G with its anti-symmetric ζ_{G_j} such as at each instant t:

$\forall i \in \mathbb{N}^*, i \leq o$:

$$\zeta_{G_i} \cup \zeta_{G_j} \Leftrightarrow S_G(t) = \mathcal{F}_G(\mathcal{G}_1, \ldots, \mathcal{G}_i, \ldots, \mathcal{G}_o) \tag{2.25}$$

where $\mathcal{F}_G$ is an arbitrary transfer function, $\mathcal{G}_i = \Delta V_{G_i} + \Delta V_{G_j}$ and ΔV_{G_i} is the EMF across the terminals of ζ_{G_i}. Similarly, we combine each receiving antennas ζ_{H_i} of ζ_H with its symmetric ζ_{H_j} such as at each instant t:

$\forall i \in \mathbb{N}^*, i \leq p$:

$$\zeta_{H_i} \cup \zeta_{H_j} \Leftrightarrow S_H(t) = \mathcal{F}_H(\mathcal{H}_1, \ldots, \mathcal{H}_i, \ldots, \mathcal{H}_p) \tag{2.26}$$

where $\mathcal{F}_H$ is an arbitrary transfer function, $\mathcal{H}_i = \Delta V_{H_i} + \Delta V_{H_j}$ and ΔV_{H_i} is the EMF across the terminals of ζ_{H_i}.

In practice, this combination can be achieved simply by connecting each ζ_{E_i} in series[1] with ζ_{E_j}, each ζ_{F_i} in series[1] with ζ_{F_j}, each ζ_{G_i} in series[1] with ζ_{G_j} and each ζ_{H_i} in series[1] with ζ_{H_j}.

Proof

Given $\zeta_{E_i} \overset{\vec{n},\vec{A}}{\rightleftharpoons} \zeta_{E_j}$, $\zeta_{F_k} \overset{\vec{n},\vec{A}}{\rightleftharpoons} \zeta_{F_l}$, $\zeta_{G_i} \overset{\vec{n},\vec{A}}{\rightleftharpoons} \zeta_{G_j}$, $\zeta_{H_k} \overset{\vec{n},\vec{A}}{\rightleftharpoons} \zeta_{H_l}$, and based on relations (2.13), (2.14) and (3.18) every $\mathcal{G}_i$ can be expressed as a function of the input signals $S_E(t)$ and $S_F(t)$ so that:

$\forall i \in \mathbb{N}^{2*}, i \leq o :$

$$\begin{aligned}
\mathcal{G}_i &= \Delta V_{G_i} + \Delta V_{G_j} \\
&\quad + \left(\sum_{k=1}^{m} M_{G_i,E_k} \cdot \mathcal{F}_{E_k}(S_E) + M_{G_j,E_l} \cdot \mathcal{F}_{E_l}(S_E) \right) \\
&\quad + \left(\sum_{k=1}^{n} M_{G_i,F_k} \cdot \mathcal{F}_{F_k}(S_F) + M_{G_j,F_l} \cdot \mathcal{F}_{F_l}(S_F) \right) \\
\mathcal{G}_i &= 2 \sum_{k=1}^{m} M_{G_i,E_k} \cdot \mathcal{F}_{E_k}(S_E) \qquad (2.27)
\end{aligned}$$

Thus the output signal $S_G(t)$ of the anti-symmetric antenna array ζ_G is independent of the input signal $S_F(t)$.

Similarly, based on relations (2.15) and (2.16) every $\mathcal{H}_i$ can be expressed function of the input signals $S_E(t)$ and $S_F(t)$ so that:

$\forall i \in \mathbb{N}^{2*}, i \leq p :$

$$\mathcal{H}_i = 2 \sum_{k=1}^{n} M_{H_i,F_k} \cdot \mathcal{F}_{F_k}(S_F(t)) \qquad (2.28)$$

Thus the output signal $S_H(t)$ of the symmetric antenna array ζ_H is independent of the input signal $S_E(t)$.

[1] In theory parallel connection should work as well. In practice the slight differences between each antenna's Equivalent Series Resistance would require a balancing circuit to achieve perfect crosstalk cancellation. Parallel connection may thus be a more flexible combination method yet more complicated to put in application. Of course, parallel and series connection are not the only possibilities...

Partial Conclusion

Given a set of parameters $\vec{n}$ and $\vec{A}$, we show that a channel $\{S_G, S_E\}$ of $Q_{\vec{n},\vec{A}}$ anti-symmetric emitting (ζ_E) and receiving (ζ_G) arrays can, in practice, be made independent of another channel $\{S_H, S_F\}$ of $Q_{\vec{n},\vec{A}}$ symmetric emitting (ζ_F) and receiving (ζ_H) arrays using elementary combination method (series connection, parallel connection, ...).

Although the conclusion drown here is a special case encompassed by the maximal ratio combining technique (MRC) [14,15], the approach presented here is original in that it eases a lot the design process of multichannel antenna design, as we will illustrate it in the following example. More importantly, this is a fundamental element of the Pie-Chart antenna concept presented in the next section.

Example: Serial Layout

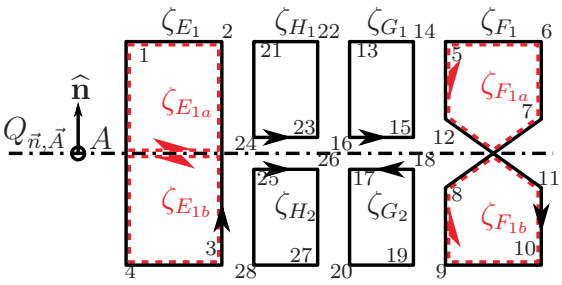

Pt	x	y	z	Pt	x	y	z	Pt	x	y	z
1	0	3.5	0	**2**	1.5	3.5	4.5	**3**	1.5	0	4.5
4	0	0	0	**5**	5	3.5	0	**6**	6.5	3.5	4.5
7	6.5	2.5	4.5	**8**	5	1	0	**9**	5	0	0
10	6.5	0	4.5	**11**	6.5	1	4.5	**12**	5	2.5	0
13	3.5	3.5	0	**14**	4.5	3.5	3	**15**	4.5	2	3
16	3.5	2	0	**17**	3.5	1.5	0	**18**	4.5	1.5	3
19	4.5	0	3	**20**	3.5	0	0	**21**	2	3.5	0
22	3	3.5	3	**23**	3	2	3	**24**	2	2	0
25	2	1.5	0	**26**	3	1.5	3	**27**	3	0	3
28	2	0	0	**A**	-1	1.75	0	$\hat{\mathbf{n}}$	0	1	0

Figure 2.2: Arbitrary symmetric and anti-symmetric arrays of antennas. Arrows indicate the antenna's orientation. 3D coordinates of the points 1 to 28 are expressed in meters. Notice that ζ_{E_1} and ζ_F are homeomorphic to their symmetric/anti-symmetric. For a better visualization of the situation, they can be seen as the serial combination of the manifold red dashed paths $\zeta_{E_{1a}}$ and $\zeta_{E_{1b}}$, respectively $\zeta_{F_{1a}}$ and $\zeta_{F_{1b}}$.

Lets consider the emitting arrays $\zeta_E = \zeta_{E_1}$ and $\zeta_F = \zeta_{F_1}$ and the receiving arrays $\zeta_G = \zeta_{G_1} \cup \zeta_{G_2}$ and $\zeta_H = \zeta_{H_1} \cup \zeta_{H_2}$ illustrated on Fig. 2.2. They are connected in serial to their input/output signal as illustrated on Fig. 2.3. Paths are made of isotropic homogenous conductive material of 5 mm radius circular cross section. ζ_E and ζ_G are $Q_{\vec{n},\vec{A}}$ anti-symmetric arrays, ζ_F and ζ_H are $Q_{\vec{n},\vec{A}}$ symmetric ones. The conveniently built *matrix of inductance* [21], numerically evaluated using the Neumann Equation (2.7), is

provided in the table associated with the Figure 2.3.

$S_E(t)$, $S_F(t)$, $S_G(t)$ and $S_H(t)$ are measured (receiver) or imposed (emitter) time-dependent EMF signals. Each signal can be expressed function of the others. For example:

$$\begin{aligned} S_E(t) &= \Delta V_{R_E} + \Delta V_{E_1} \\ &= i_E \cdot R_E \\ &\quad + M_{E,E} \cdot \frac{d\ i_E(t)}{dt} \\ &\quad + M_{E,F} \cdot \frac{d\ i_F(t)}{dt} \\ &\quad + (M_{E,G_1} + M_{E,G_2}) \cdot \frac{d\ i_G(t)}{dt} \\ &\quad + (M_{E,H_1} + M_{E,H_2}) \cdot \frac{d\ i_H(t)}{dt} \end{aligned} \tag{2.29}$$

Repeating this process for every antennas and given the inductance in Table 2.1.2, expressions obtained for each signal are reduced to:

$$\begin{aligned} S_E(t) &= i_E \cdot R_E + M_{E,E} \cdot \frac{d\ i_E}{dt} \\ &\quad + (M_{E,G_1} + M_{E,G_2}) \cdot \frac{d\ i_G}{dt} \end{aligned} \tag{2.30}$$

$$\begin{aligned} S_F(t) &= i_F \cdot R_F + M_{F,F} \cdot \frac{d\ i_E}{dt} \\ &\quad + (M_{F,H_1} + M_{F,H_2}) \cdot \frac{d\ i_H}{dt} \end{aligned} \tag{2.31}$$

$$\begin{aligned} S_G(t) &= i_G \cdot R_G + (M_{G_1,G_1} + M_{G_2,G_2}) \cdot \frac{d\ i_G}{dt} \\ &\quad + (M_{G_1,E} + M_{G_2,E}) \cdot \frac{d\ i_E}{dt} \end{aligned} \tag{2.32}$$

$$\begin{aligned} S_H(t) &= i_H \cdot R_H + (M_{H_1,H_1} + M_{H_2,H_2}) \cdot \frac{d\ i_H}{dt} \\ &\quad + (M_{H_1,F} + M_{H_2,F}) \cdot \frac{d\ i_F}{dt} \end{aligned} \tag{2.33}$$

The above studied system is thus equivalent to an inductive transmission device having two independent channels: the "anti-symmetric" channel $Ch1 = \{\zeta_E, \zeta_G\}$ and the "symmetric" channel $Ch2 = \{\zeta_F, \zeta_H\}$.

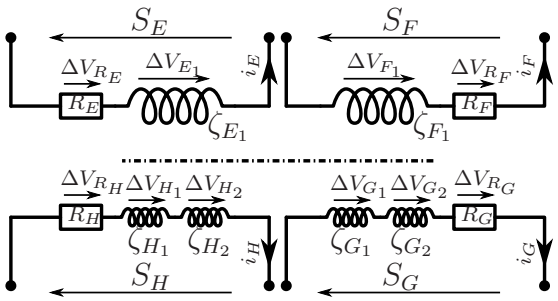

(µH)	$M_{E_1,j}$	$M_{F_1,j}$	$M_{G_1,j}$	$M_{G_2,j}$	$M_{H_1,j}$	$M_{H_2,j}$
M_{i,E_1}	20.10	0.000	0.183	0.183	0.441	-0.441
M_{i,F_1}	0.000	27.21	0.398	-0.398	0.066	0.066
M_{i,G_1}	0.183	0.398	10.11	-0.335	0.423	-0.018
M_{i,G_2}	0.183	-0.398	-0.335	10.11	0.018	-0.423
M_{i,H_1}	0.441	0.066	0.423	0.018	10.11	0.335
M_{i,H_2}	-0.441	0.066	-0.018	-0.423	0.335	10.11

Figure 2.3: Electric circuit of the simple 2 channels inductive transmission device presented Fig. 2.2 (left picture) and the associated inductance matrix numerically evaluated (right table). In this example, antennas ζ_{H_1} and ζ_{H_2} of the ζ_H array are combined in a serial fashion. Same goes for the antennas of the ζ_G array.

2.2 Pie-Chart Antenna Model

2.2.1 Iterative Building Process

Lets consider a plane $Q_{\vec{n},\vec{A}}$ and a vector $\vec{n}_0$ perpendicular to $\vec{n}$. We recursively construct any vector $\vec{n}_i$ parallel to $Q_{\vec{n},\vec{A}}$ so that $\widehat{\mathbf{n}}_{i+1}$ is the vector resulting from the rotation of $\widehat{\mathbf{n}}_i$ around the $(O:\vec{n})$ axis by an angle $\theta_{i+1} = \frac{\pi}{2^{i+1}}$. Hence $\vec{n}_{i+1}$ satisfies:

$$\widehat{\mathbf{n}}_{i+1} = [\mathbf{R}]^{\widehat{\mathbf{n}}}_{\theta_{i+1}} \times \widehat{\mathbf{n}}_i \tag{2.35}$$

where $\widehat{\mathbf{n}} = \frac{\vec{n}}{\|\vec{n}\|}$ and $[\mathbf{R}]^{\widehat{\mathbf{n}}}_{\theta_{i+1}}$ is the rotation matrix (2.34). In our case, this is equivalent to:

$$\forall i \in \mathbb{N}, \left| \begin{array}{rcl} \vec{n}_i & \neq & \vec{0} \\ \widehat{\mathbf{n}} \cdot \widehat{\mathbf{n}}_0 & = & 0 \\ \widehat{\mathbf{n}}_i \times \widehat{\mathbf{n}}_{i+1} & = & -\sin(\theta_{i+1})\widehat{\mathbf{n}} \\ \widehat{\mathbf{n}}_i \cdot \widehat{\mathbf{n}}_{i+1} & = & \cos(\theta_{i+1}) \end{array} \right. \tag{2.36}$$

Lets consider an arbitrary elemental array ξ_X. We construct an m order Pie-Chart array ζ^m_X by recursively applying the symmetry function Z as follow (Fig. 2.4):

$\forall m \in \mathbb{N}^*, \forall i < m, i \in \mathbb{N}^*$:

$$\left| \begin{array}{rcl} \zeta^m_{X(0)} & = & \xi_X \\ \zeta^m_{X(i)} & = & \zeta^m_{X(i-1)} \cup \overset{\vec{n}_{i-1},\vec{A}}{\rightleftharpoons} \zeta^m_{X(i-1)} \\ \zeta^m_X & = & \zeta^m_{X(m)} = \zeta^m_{X(m-1)} \cup \overset{\vec{n}_{m-1},\vec{A}}{\rightleftharpoons} \zeta^m_{X(m-1)} \end{array} \right. \tag{2.37}$$

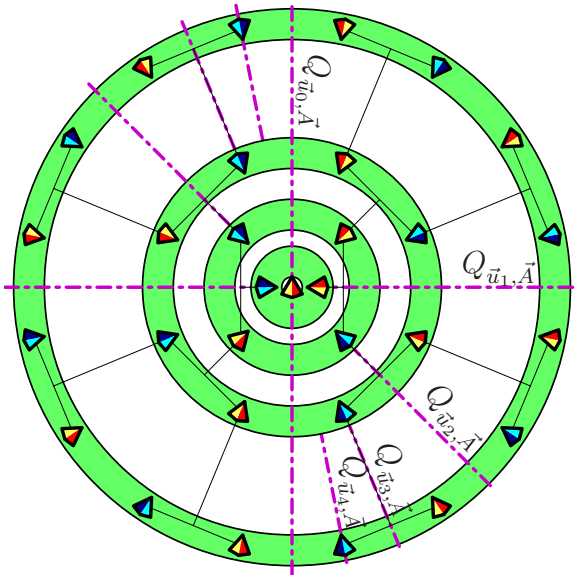

Figure 2.4: This radial fractal tree is an intuitive way to visualize the geometric building process of any n order Pie-Chart array. Reading starts at the center with the geometry of a 1^{st} order Pie-Chart antenna, result of the union of a red triangle with its yellow anti-symmetric one about the $Q_{\vec{u}_0,\vec{A}}$ plane (point A is the center of the figure). Progressing on the first green ring (the smallest one), the geometry of a 2^{nd} order array is composed of two antennas, result of the union of a red triangle and its blue symmetric about the $Q_{\vec{u}_0,\vec{A}}$ plane with their yellow and cyan anti-symmetric one about the $Q_{\vec{u}_1,\vec{A}}$ plane. And so on and so forth. Therefore, antennas on the most outer green ring can be combined into a 5^{th} order Pie-Chart array. In practice, red/yellow figures are combined with the blue/cyan one so that current flowing through red/yellow figures flows in the opposite direction of that flowing through blue/cyan ones.

$$[\mathbf{R}]^{\widehat{\mathbf{n}}}_{\theta_{i+1}} = \begin{bmatrix} n_x^2(1-C)+C & n_xn_y(1-C)-n_zS & n_xn_z(1-C)+n_yS \\ n_xn_y(1-C)+n_zS & n_y^2(1-C)+C & n_yn_z(1-C)-n_xS \\ n_xn_z(1-C)-n_yS & n_yn_z(1-C)+n_xS & n_z^2(1-C)+C \end{bmatrix} \tag{2.34}$$

where $C = \cos(\theta_{i+1})$ and $S = \sin(\theta_{i+1})$.

2.2.2 Proof of the Crosstalk Cancellation

- Suppose that $Q_{\vec{n}_i,\vec{A}}$ is the median plane between $Q_{\vec{n}_{i-1},\vec{A}}$ and $Q_{\vec{n}_0,\vec{A}}$ such as $-\vec{n}_0 = \overbrace{\vec{n}_{i-1}}^{\vec{n}_i,\vec{0}}$. Then based on (2.36) we deduce the following:

$$\left| \begin{array}{rcl} \widehat{\mathbf{n}}_i \times \widehat{\mathbf{n}}_0 & = & -\sin(\theta_i)\widehat{\mathbf{n}} \\ \widehat{\mathbf{n}}_i \cdot \widehat{\mathbf{n}}_0 & = & \cos(\theta_i) \end{array} \right. \tag{2.38}$$

which is equivalent to:

$$\widehat{\mathbf{n}}_0 = [\mathbf{R}]^{\widehat{\mathbf{n}}}_{\theta_i} \times \widehat{\mathbf{n}}_i \tag{2.39}$$

Taking notice that $\theta_{i+1} = \theta_i/2$ and remembering that $\widehat{\mathbf{n}}_{i+1} = [\mathbf{R}]^{\widehat{\mathbf{n}}}_{\theta_{i+1}} \times \widehat{\mathbf{n}}_i$, we can deduce that $\widehat{\mathbf{n}}_0 = [\mathbf{R}]^{\widehat{\mathbf{n}}}_{\theta_i/2} \times ([\mathbf{R}]^{\widehat{\mathbf{n}}}_{\theta_i/2} \times \widehat{\mathbf{n}}_i) = [\mathbf{R}]^{\widehat{\mathbf{n}}}_{\theta_{i+1}} \times \widehat{\mathbf{n}}_{i+1}$. Therefore $Q_{\vec{n}_{i+1},\vec{A}}$ is the median plane between $Q_{\vec{n}_i,\vec{A}}$ and $Q_{\vec{n}_0,\vec{A}}$ such as $-\widehat{\mathbf{n}}_0 = Z(\widehat{\mathbf{n}}_i, \vec{n}_{i+1}, \vec{0})$.

- Based on (2.36) we know that $\widehat{\mathbf{n}}_1 = [\mathbf{R}]^{\widehat{\mathbf{n}}}_{\pi/2} \times \widehat{\mathbf{n}}_0$, thus giving $-\widehat{\mathbf{n}}_0 = [\mathbf{R}]^{\widehat{\mathbf{n}}}_{\pi/2} \times \widehat{\mathbf{n}}_1$. This is equivalent to say that $Q_{\vec{n}_1,\vec{A}}$ is the median plane between $Q_{\vec{n}_0,\vec{A}}$ and $Q_{\vec{n}_0,\vec{A}}$ such as $-\widehat{\mathbf{n}}_0 = Z(\widehat{\mathbf{n}}_i, \vec{n}_{i+1}, \vec{0})$.

We can thus deduce that the last building plane of symmetry $Q_{\vec{n}_i,\vec{A}}$ of a Pie-Chart array is the median plane between $Q_{\vec{n}_{i-1},\vec{A}}$ and $Q_{\vec{n}_0,\vec{A}}$ such as $-\vec{n}_0 = Z(\vec{n}_{i-1}, \vec{n}_i, \vec{0})$.

Lets consider a body Ω_a mirror symmetric about two planes $Q_{\vec{n}_a,\vec{A}}$ and $Q_{\vec{n}_b,\vec{A}}$, and the body Ω_b defined by $\Omega_b = Z(\Omega_a, \vec{n}_c, \vec{A})$. Given that Z is an isometry of the euclidean space, we can conclude that Ω_b is mirror symmetric about the two planes $Z(Q_{\vec{n}_a,\vec{A}}, \vec{n}_c, \vec{A})$ and $Z(Q_{\vec{n}_b,\vec{A}}, \vec{n}_c, \vec{A})$.

Lets set $\vec{n}_c$ so that $Q_{\vec{n}_c,\vec{A}}$ is a median plane between $Q_{\vec{n}_a,\vec{A}}$ and $Q_{\vec{n}_b,\vec{A}}$. This either means that $\widehat{\mathbf{n}}_a = \overset{\vec{n}_c,\vec{0}}{\widetilde{\widehat{\mathbf{n}}}}_b$ or $-\widehat{\mathbf{n}}_a = \overset{\vec{n}_c,\vec{0}}{\widetilde{\widehat{\mathbf{n}}}}_b$, thus resulting in:

$$\overset{\vec{n}_c,\vec{A}}{\widetilde{Q}}_{\vec{n}_a,\vec{A}} = Q_{\vec{n}_b,\vec{A}} \tag{2.40}$$

Indeed Ω_b stays mirror symmetric about the planes $Q_{\vec{n}_a,\vec{A}}$ and $Q_{\vec{n}_b,\vec{A}}$. Applying this result to oriented paths, we can conclude that:

$$\zeta_m = \overset{\vec{n}_{m-2},\vec{A}}{\overleftrightarrows}\zeta_m = \overset{\vec{n}_0,\vec{A}}{\overleftrightarrows}\zeta_m = \overset{\vec{n}_{m-1},\vec{A}}{\overleftrightarrows}\zeta_m \tag{2.41}$$

This same statement also means that ζ_m admits $\overset{\vec{n}_{m-2},\vec{A}}{\widetilde{Q}}_{\vec{n}_{m-1},\vec{A}}$ as a plane of symmetry, as well as $Z(\overset{\vec{n}_{m-2},\vec{A}}{\widetilde{Q}}_{\vec{n}_{m-1},\vec{A}}, \overset{\vec{n}_{m-2},\vec{A}}{\widetilde{n}}_{m-1}, \vec{A})$, etc.. Indeed symmetry planes of ζ_m are defined at a rotation $[\mathbf{R}]^{\widehat{\mathbf{n}}}_{i\theta_{m-2}}$ of $Q_{\vec{n}_{m-2}}$, and antisymmetry planes at a rotation $[\mathbf{R}]^{\widehat{\mathbf{n}}}_{i\theta_{m-2}}$ of $Q_{\vec{n}_{m-1}}$. Remembering that $\theta_{i+1} = \theta_i/2$, then $\forall i \in [1; m]$, $Q_{\vec{n}_{m-i},\vec{A}}$ is a plane of antisymmetry of ζ_m. Which allows us to say:

Any m order Pie-Chart *array* ζ_m *is decoupled with any lower order* Pie-Chart *array sharing the same building parameters* $\vec{A}$, $\widehat{\mathbf{n}}$ *and* $\widehat{\mathbf{n}}_0$.

2.3 Experiments

In the following section we present two of the experiments we conducted to evaluate the applicability of the above theoretical model.

2.3.1 Three-channels PCB Pie-Chart Array

The use of symmetry to reduce inductive crosstalk is a well known technique [17]. However, up to current literature, this technique alone seems effective up to a maximum of 2 independent channels per axis (i.e., a maximum of 6 channels in a 3D space). In the following experiments, we measure how effective is the proposed *Pie-Chart* antenna concept to overcome this limit of 2 independent channels per axis.

Design and Manufacture

For speed and accuracy reasons, we decided to make the antennas by the mean of PCB etching. Insulation is ensured by a layer of about 0.1 mm thick rubber. We designed the antennas based on the following requirements:

- at least 3 coplanar channels, because 2 coplanar channels case is part of common knowledge, well documented and used in various applications.
- self-inductance of every antennas must be close in order to lower the probability that the observed crosstalk attenuation is due to a difference between channel's pass-band frequency.
- given the characteristics of the used power supply (50 Ω ±10 V, up to 15 MHz sinusoidal waveform generator), antenna's self-inductance and electrical length must be chosen so that antennas are exploitable at frequencies lower than 15 MHz (≃20 m long wavelength).

Therefore we needed a mean to evaluate the inductance matrix of the system while designing the antennas. For this purpose, we wrote a rudimentary computer program (cf. Appendix B) which returns the mutual inductance between any pair of arbitrary geometry antennas based on Neumann Equation (2.7). The final circuit shown Fig. 2.5 were etched on a standard 35 µm copper plated 150 × 100mm large 1.6 mm thick glass Fiber Reinforced Epoxy board and thin-coated with rubber as illustrated on Fig. 2.6.

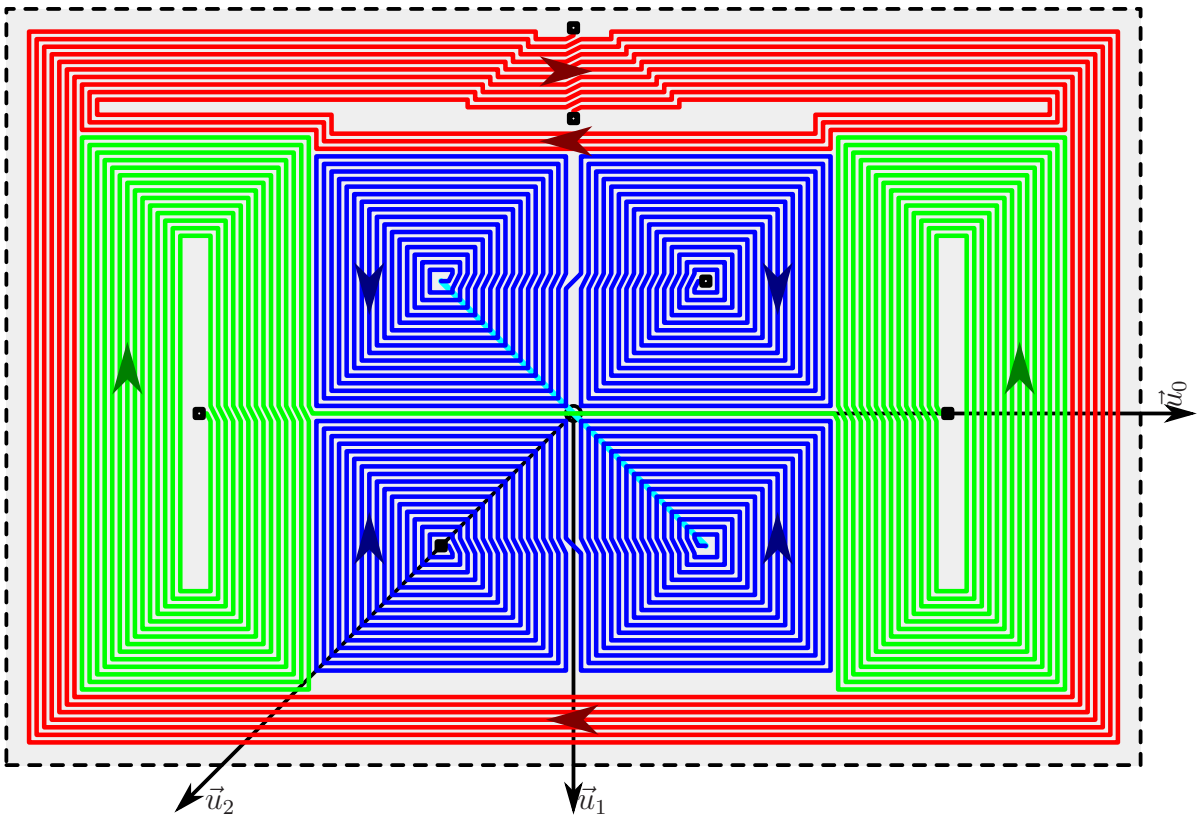

Figure 2.5: Tracks of the experimental PCB Pie-Chart array. 1st channel is composed of the 1st order red Pie-Chart antenna, 2nd channel is composed of the 2nd order green Pie-Chart antenna and the 3rd channel is composed of the 3rd order blue Pie-Chart antenna. Colored arrows indicate the orientation of the current inside the corresponding antenna. Vector $\vec{u}_0$, $\vec{u}_1$ and $\vec{u}_2$ are the normals of the construction planes $Q_{\vec{n}_0,\vec{A}}$ to $Q_{\vec{n}_2,\vec{A}}$. Small black squares are the antenna's terminals. Cyan line represents a link on the rear side of the PCB. Black dashed rectangle is the 150 × 100mm outer limit of the PCB.

Numerical Results

We consider a stack of the above presented two tri-channel arrays: one PCB is put up-side-down on top of the other and separated by a distance $h = 1\,\text{mm}$ as shown at the top right corner of the photograph Fig. 2.6. The numerically evaluated inductance matrix is given in the table of the Fig. 2.6 given that ζ_{Bi} is the ith channel of the bottom PCB array and ζ_{Ti} is the ith channel of the top PCB array.

The highlighted main diagonal shows that the self-inductance of each antenna is close to 14 µH. Lightly highlighted second diagonals shows that each co-channel's mutual inductance, about 12 µH, is closed to antennas self-inductance. Given the formula (2.42)

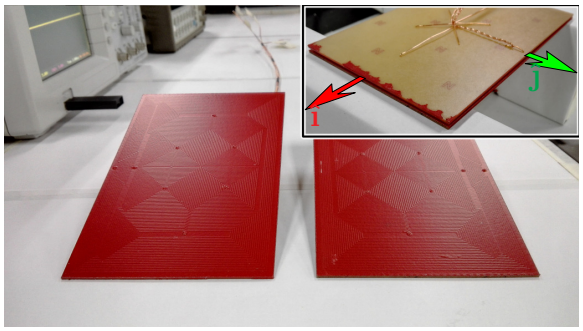

(µH)	$M_{B1,j}$	$M_{B2,j}$	$M_{B3,j}$	$M_{T1,j}$	$M_{T2,j}$	$M_{T3,j}$
$M_{i,B1}$	17.69	-0.004	0.004	-15.29	-0.004	-0.003
$M_{i,B2}$	-0.004	18.00.	-0.017	-0.004	15.23	-0.017
$M_{i,B3}$	0.004	-0.017	18.21	-0.003	-0.017	15.06
$M_{i,T1}$	-15.29	-0.004	-0.003	17.69	-0.004	0.004
$M_{i,T2}$	-0.004	15.23	-0.017	-0.004	18.00	-0.017
$M_{i,T3}$	-0.003	-0.017	15.06	0.004	-0.017	18.21

Figure 2.6: Photograph of the experimental 3 channels PCB type Pie-Chart array (left picture) and the associated inductance matrix numerically evaluated (right table). Circuit tracks presented Fig. 2.5 were etched on two 150 × 100mm boards. Those PCB were then coated with a thin layer of colored rubber (red surface). Unit vectors $\hat{\mathbf{i}}$ of the X axis and $\hat{\mathbf{j}}$ of the Y axis are indicated on the top right corner image in testing configuration (i.e., one PCB flipped upside down on top of the other PCB about the Y axis).

[18], we can thus expect a minimum co-channel magnetic coupling factor $\min(k_{co}) = k_{B1,T1} = 86\,\%$.

$$\forall (i,j) \in \mathbb{N} : k_{i,j} = \sqrt{\frac{M_{i,j}^2}{M_{i,i} \times M_{j,j}}} \tag{2.42}$$

In comparison, the evaluated cross-channel's mutual inductances are not higher than 10 nH. Therefore, we can expect a maximum cross-channel magnetic coupling factor of $\max(k_{cross}) = k_{B1,B3} = 7.2 \times 10^{-2}\,\%$. In this configuration, assuming that the transmission of power is approximately proportional to k^2 [19], this corresponds to an expected minimal Adjacent Channel Rejection Ratio (ACRR, selectivity or signal to noise power ratio) $\min(\mathcal{S}_{i,j}) = \mathcal{S}_{B3,T2} \simeq 59\,\text{dB}$ given[2]:

$$\mathcal{S}_{i,j} = \min\left(20\log_{10}\left(\frac{k_{i1,i2}}{k_{i1,j}}\right) \right) \tag{2.43}$$

where antennas ζ_{i1} and ζ_{i2} are two different antennas of the channel i and ζ_j is an antenna of the channel j. Notice that this equation leads to $\mathcal{S}_{i,j} \propto (M_{j,j}/M_{i,i})^{1/2}$. From a crosstalk reduction stand point, this means that a given multichannel inductive system would generally benefit from designing higher power channels with proportionally higher

[2]Based on (2.42), $M_{i,j} = M_{j,i}$ implies $k_{i,j} = k_{j,i}$; however, regarding (2.43), this does NOT imply that $\mathcal{S}_{i,j} = \mathcal{S}_{j,i}$.

self-inductance than lower power channels.

The same evaluation procedure was repeated in different configurations. Fig. 2.7 illustrates the expected evolution of the minimum ACRR between channels function of the PCB misalignment (translation only) along the x, y and z axis.

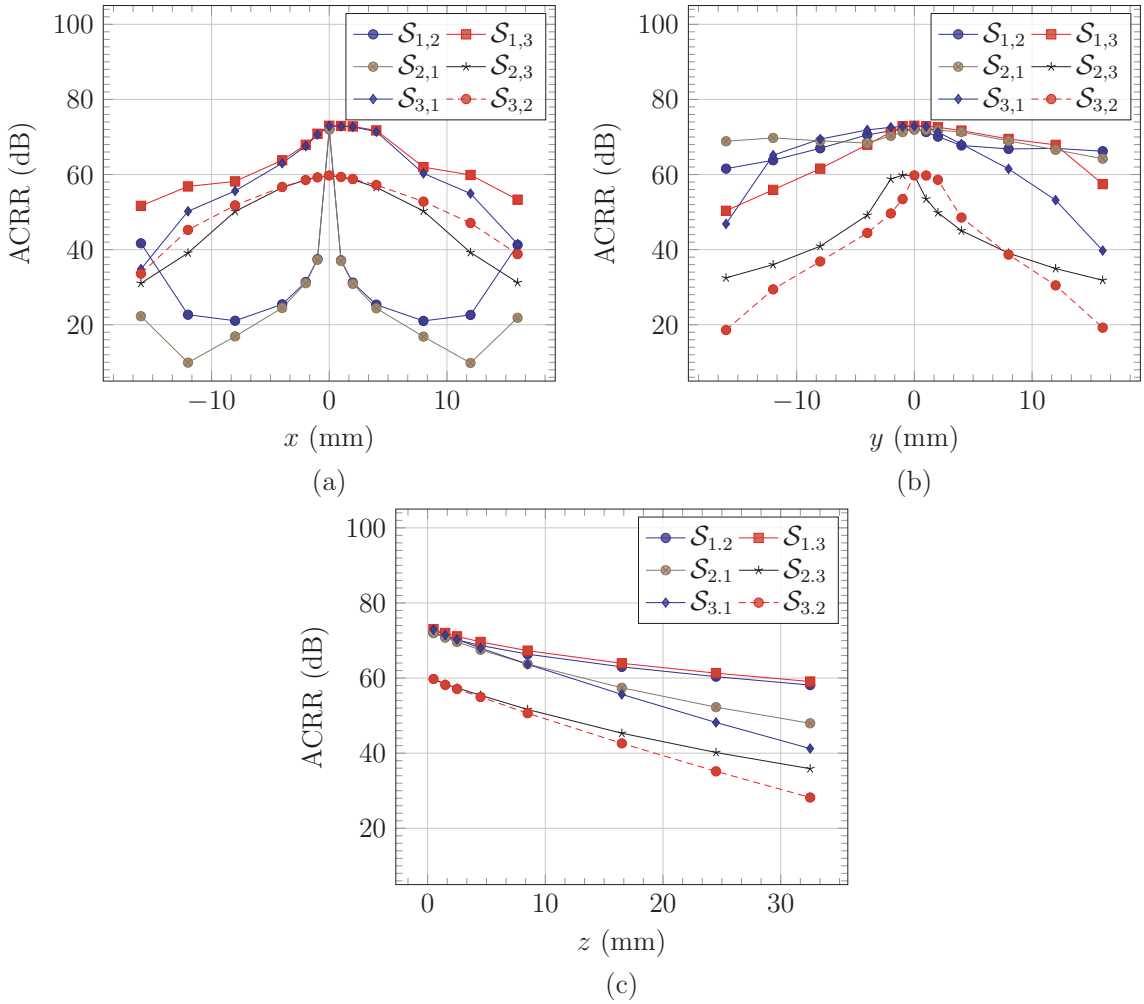

Figure 2.7: Numerically evaluated impact of the PCB array misalignment along the x (a), y (b) and z axis (c) on the Adjacent Channel Rejection Ratio (ACRR).

Experimental Setup

We would like to experimentally determine the ACRR and the mutual inductance matrix of the system at position $(0, 0, 1)_{O;\hat{\mathbf{i}},\hat{\mathbf{j}},\hat{\mathbf{k}}}$ (no x, y misalignment, 1 mm gap).

An antenna can be configured on the fly as emitter (connected to power supply) or receiver (disconnected to power supply) thanks to the routing circuit shown Fig. 2.8.

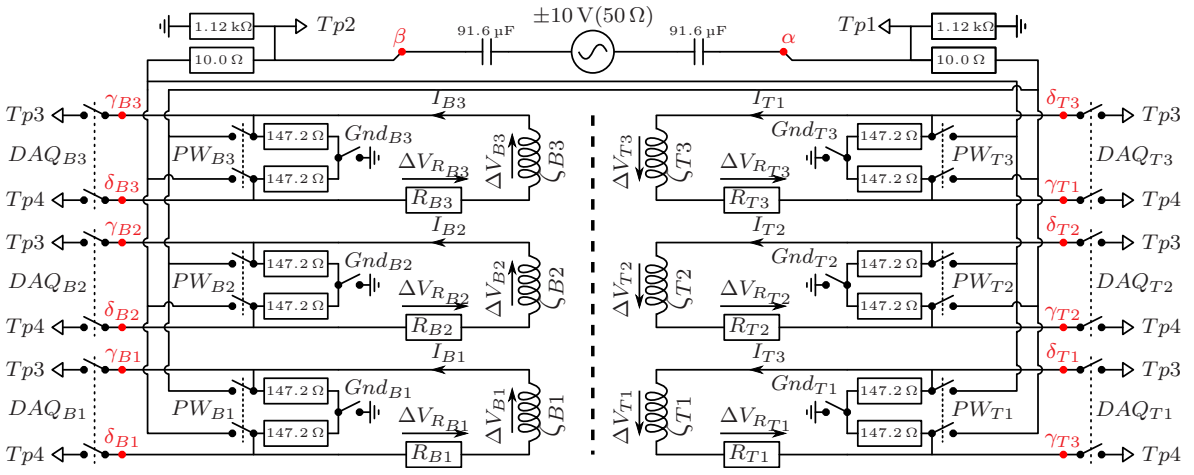

Figure 2.8: Routing circuit for experimental evaluation of up to 6 antenna system's inductance matrix. Signal supplied by the AC generator through 91.6 µF ceramic coupling capacitors is balanced with a pair of 1.12 kΩ resistors. It is then routed to only one emitting antenna ζ_i by closing the switches PW_i (configuration XP_i). Probed points $\{\alpha, \beta\}$ are connected to oscilloscope's 1st and 2nd inputs ($Tp1$ and $Tp2$). Probed points $\{\gamma_{B1}, \delta_{B1}\}$ to $\{\gamma_{T3}, \delta_{T3}\}$ are pairwise routable to the 3rd and 4th inputs of the oscilloscope ($Tp3$ and $Tp4$) via the switches DAQ_{B1} to DAQ_{T3}. A complete data set consists of a record of $\{\alpha, \beta, \gamma_{B1}, \delta_{B1}\}$ to $\{\alpha, \beta, \gamma_{T3}, \delta_{T3}\}$ for each configuration XP_i (6 configurations). For safety reasons and measurement consistency, given a configuration XP_i, when a signal $\Delta\gamma_j\delta_j$ $(j \neq i)$ is being measured, the switch Gnd_j is closed to balance the signal (Gnd switches are otherwise open). All represented ground points are oscilloscope's ground (independent from generator's ground). 1.12 kΩ, 10.0 Ω and 147.2 Ω resistors are thin film carbon resistors. $\Delta\alpha\beta$ is the time reference signal of each $\{\alpha, \beta, \gamma_x, \delta_x\}$ record.

Resistor R_i represents the Equivalent Series Resistance (ESR) of the antenna ζ_i. Their value are given in Table A.1 of the Appendix.

Given the circuit presented Fig. 2.8 and assuming that components properties are not significantly altered over the 150 Hz to 15 MHz frequency range, we can deduce the

$$5888\times[\boldsymbol{\Delta\gamma\delta}]-[\mathbf{R}]\times(294.4\,[\boldsymbol{\Delta\alpha\beta}]-314.4\,[\boldsymbol{\Delta\gamma\delta}])=[\mathbf{M}]\times\frac{d\,(294.4\,[\boldsymbol{\Delta\alpha\beta}]-314.4\,[\boldsymbol{\Delta\gamma\delta}])}{dt} \tag{2.45}$$

$$\begin{aligned}
5888\begin{bmatrix} \overset{XP_{B1}}{\downarrow} & & \overset{XP_{T3}}{\downarrow} \\ \Delta\gamma\delta_{B1} & \cdots & \Delta\gamma\delta_{B1} \\ \vdots & & \vdots \\ \Delta\gamma\delta_{T3} & & \Delta\gamma\delta_{T3} \end{bmatrix} - \begin{bmatrix} R_{B1} & & 0 \\ & \ddots & \\ 0 & & R_{T3} \end{bmatrix} \times \left(294.4 \begin{bmatrix} \Delta\alpha\beta & \cdots & \Delta\gamma\delta_{B1} \\ \vdots & \ddots & \vdots \\ \Delta\gamma\delta_{T3} & & \Delta\alpha\beta \end{bmatrix} - 314.4 \begin{bmatrix} \Delta\gamma\delta_{B1} & \cdots & \Delta\gamma\delta_{B1} \\ \vdots & & \vdots \\ \Delta\gamma\delta_{T3} & & \Delta\gamma\delta_{T3} \end{bmatrix} \right) \\
= \begin{bmatrix} M_{B1,B1} & \cdots & M_{T3,B1} \\ \vdots & \ddots & \\ M_{B1,T3} & & M_{T3,T3} \end{bmatrix} \times \frac{d}{dt} \left(294.4 \begin{bmatrix} \Delta\alpha\beta & \cdots & \Delta\gamma\delta_{B1} \\ \vdots & \ddots & \vdots \\ \Delta\gamma\delta_{T3} & & \Delta\alpha\beta \end{bmatrix} - 314.4 \begin{bmatrix} \Delta\gamma\delta_{B1} & \cdots & \Delta\gamma\delta_{B1} \\ \vdots & & \vdots \\ \Delta\gamma\delta_{T3} & & \Delta\gamma\delta_{T3} \end{bmatrix} \right)
\end{aligned}$$

$$\begin{aligned}
[\mathbf{M}] = (5888 \times [\boldsymbol{\Delta\gamma\delta}] - [\mathbf{R}] \times (294.4\,[\boldsymbol{\Delta\alpha\beta}] - 314.4\,[\boldsymbol{\Delta\gamma\delta}])) \\
\times \left[\frac{d\,(294.4\,[\boldsymbol{\Delta\alpha\beta}] - 314.4\,[\boldsymbol{\Delta\gamma\delta}])}{dt} \right]^{-1}
\end{aligned} \tag{2.46}$$

relation:

$$\begin{aligned}
\Delta V_{B1} &= \Delta\delta\gamma_{B1} - R_{B1}\frac{294.4\Delta\beta\alpha - 314.4\Delta\delta\gamma_{B1}}{5888} \\
&= \Delta\delta\gamma_{B1} - R_{B1}(\frac{\Delta\beta\alpha}{314.4} - \frac{\Delta\delta\gamma_{B1}}{294.4}) \\
&= \sum M_{i,B1}\frac{d\ I_i}{dt}
\end{aligned} \tag{2.44}$$

where $\Delta\delta\gamma_{B1}$ is the electric potential difference $\gamma_{B1}-\delta_{B1}$ and $\Delta\beta\alpha$ the difference $\alpha-\beta$. This assumes that ζ_{B1} is in emitter mode. When ζ_{B1} is in receiver mode, we simply consider that $\Delta\beta\alpha=\Delta\delta\gamma_{B1}$ in Equation (2.44). Same goes for the five other antennas. Hence, by recording the electric potential $\{\alpha,\beta,\gamma_{B1},\delta_{B1}\}$ to $\{\alpha,\beta,\gamma_{T3},\delta_{T3}\}$ for 6 independent emitter/receiver configurations, namely configuration XP_{B1} to XP_{T3}, we can deduce the relations (2.45) and (2.46).

In practice, configuration XP_i consisted in setting only the antenna ζ_i as an emitter, the five others being set as receivers. This minimizes the risk of non reversibility of the matrix $d(294.4\,[\boldsymbol{\Delta\alpha\beta}]-314.4\,[\boldsymbol{\Delta\gamma\delta}])/dt$.

Measurement points Tp_1 to Tp_4 were connected to the 1 MΩ inputs of a 4 channels oscilloscope (ref: Agilent 2024A) via 1.2 m unterminated crocodile clip ended 50 Ω coax-

ial cable, as can be seen on Fig. 2.9. All four coaxial cables were twisted in one strand between the measurement points and the oscilloscope inputs to reduce ground loops. Measurements were performed inside an anechoic chamber at 20 °C.

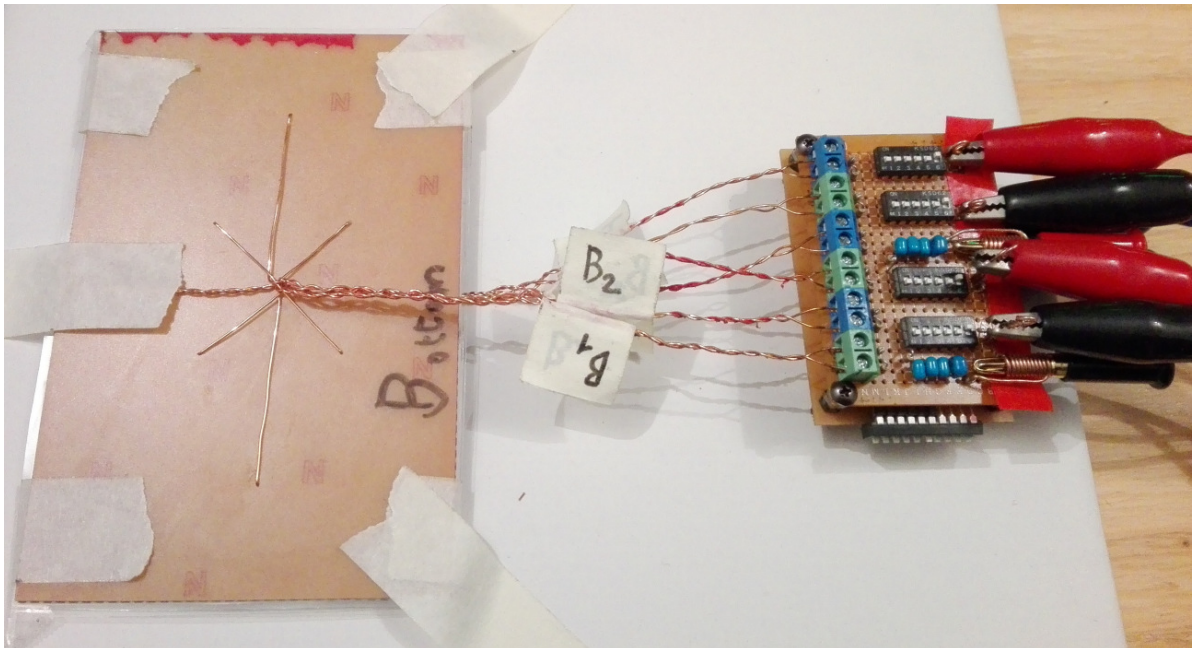

Figure 2.9: View of the PCB array experimental setup. On the left the Device Under Test (DUT), on the right the board used for routing power to the desired antenna and signal to the oscilloscope's inputs. Equivalent circuitry achieved with this board is depicted Fig. 2.8.

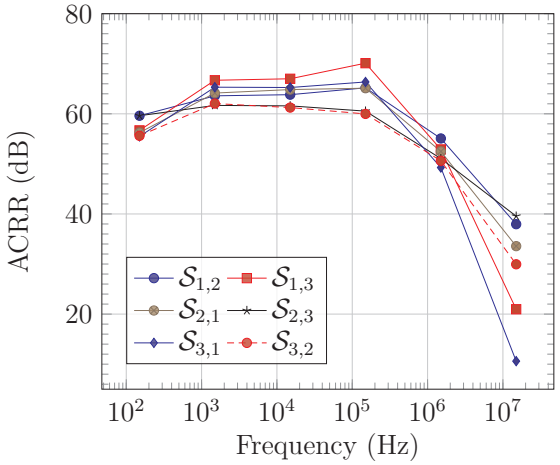

Figure 2.10: ACRR of PCB array calculated from experiment data at different frequencies.

Results

Net electric power P_j received by the $294.4\,\Omega + R_j$ load of an antenna ζ_j is accessible via the electric current matrices $[\mathbf{I\zeta}]$ (Cf. Table A.9 to Table A.14 in Appendix) by the relation $P_j = (294.4 + R_j){I\zeta_j}^2$. Assuming that crosstalk is globally low between every channels, which is apparently the case up to 1.5 MHz, then $\mathcal{S}_{i,j} \simeq 20\log_{10}((294.4 + R_i)I\zeta_i/((294.4 + R_j)I\zeta_j)$, where ζ_i is the antenna connected to the power source, gives a good estimation of the ACRR. Results shows a typical channel selectivity of 55 dB to 70 dB from 150 Hz to 150 kHz (Cf. Fig. 2.10).

The inductance matrices were automatically computed using an Octave script proceeding in the following manner:

- the amplitude and phase of the sinusoidal signals $\Delta\alpha\beta$ and $\Delta\gamma\delta$ were determined by fitting an ideal sinusoid to the raw signal using a bisection method with threshold of $1 \times 10^{-5\circ}$ on phase angle, 5×10^{-5} V on peak-to-peak amplitude and 1×10^{-5} V on common mode.
- those information and the measured ESR of each antenna (Cf. Appendix A Table A.1) were injected into the Equation (2.46).

Results are presented Appendix A Tables A.15 to A.20.

2.3.2 2 Channels Rotary Pie-Chart Array

The presented geometry was designed to address the main drawback of the "Circle" geometry proposed in [12]: a sensible level of interferences, even for the optimized "Circle" geometry tested in [16]. Unfortunately this last paper do not provide enough details to estimate the ACRR of their model. Our particular version is a basic rotary type of 2 channels Pie-Chart array designed to improve ACRR of rotating type of Near Field Wireless Transmission of Power and Information device (NFWTPI).

Design and Manufacture

From a time perspective, the rotary prototype was built and tested prior to the PCB one. At that time, primary design constraint was the availability of tools and materials.

As a simple proof of concept, we came out with the design depicted Fig. 2.11. Device was built using 48 mm inside/outside diameter PVC tube, of 0.35 mm core diameter insulated copper wire and a drill press. In this case, "power" channel $\{P_{in}, P_{out}\}$ was designed with a higher self inductance than the "data" channel $\{D_{in}, D_{out}\}$.

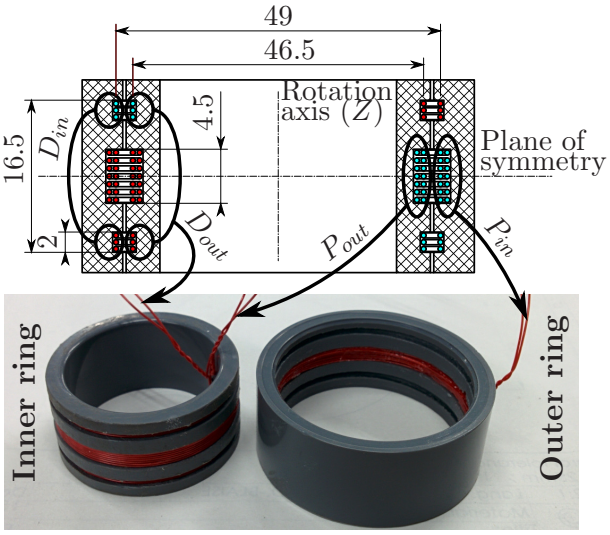

(µH)	$M_{Pin,j}$	$M_{Din,j}$	$M_{Pout,j}$	$M_{Dout,j}$
$M_{i,Pin}$	19.1016	0.0006	14.1235	0.0004
$M_{i,Din}$	0.0006	1.8618	0.0004	0.9639
$M_{i,Pout}$	14.1235	0.0004	17.2306	0.0005
$M_{i,Dout}$	0.0004	0.9639	0.0005	1.6974

Figure 2.11: Construction of the non-contact slip ring's, or rotary array (left schematic), and associated inductance matrix numerically evaluated (right table). Red and blue colors on the top cross-section differentiate the orientation of electric current inside the coils conductors. Coils P_{in} and P_{out} are each made of 14 turns of conductor, D_{in} and D_{out} are each made of 2×3 turns of conductor.

Results

Numerical results presented in the table of the Fig. 2.11 were obtained using the same methodology as that of the PCB array. Based on this table, we can expect a minimum ACRR $\mathcal{S}_{P,D}$ close to 91 dB and $\mathcal{S}_{D,P}$ close to 67 dB. Once again we present Fig. 2.12 the expected evolution of ACRR $\mathcal{S}_{i,j}$ function of misalignment along the rotation axis (Z axis). Fig. 2.13 shows the ACRR evaluated from the experimental results. Evaluated inductance matrices presented in Appendix A Tables A.21 to A.26 were obtained using similar procedure as that of the PCB array. Measured ESR used in those calculations are presented in Appendix A Table A.2 and the current through the inductors are presented in Table A.3 to A.8.

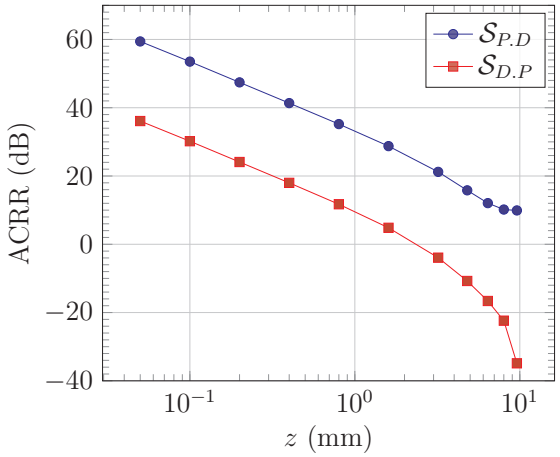

Figure 2.12: Numerically evaluated impact of the rotary array misalignment along the z axis on the ACRR.

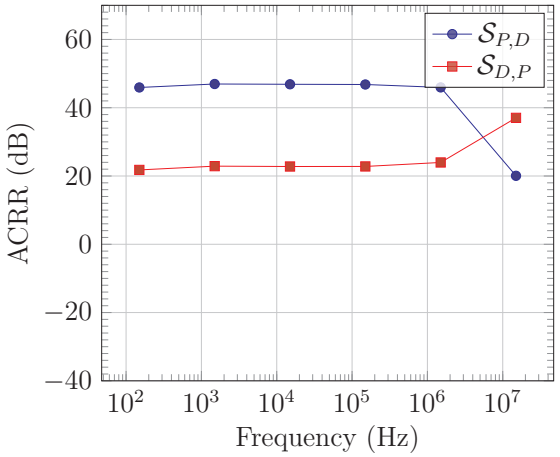

Figure 2.13: ACRR of rotary array calculated from experiment data at different frequencies.

2.4 Discussion

Experimental results globally agree with the theory: we observe a significant ACRR in most of the tested configurations. However there are several discrepancies that we will discuss in this section.

2.4.1 Symmetry of the Inductance Matrices

Up to Neumann formula, the inductance matrices should be symmetric. Lets define a coefficient W which qualifies how symmetric is a given square matrix $[\mathbf{M}]$ of size n. W is equal to 1 minus the average ratio of the difference between two diagonally opposed terms over the range of all non-diagonal terms such as:

$$W = 1 - \frac{2}{n^2 - n} \sum_{i=2}^{n} \sum_{j=1}^{i-1} \frac{|(M_{i,j} - M_{j,i}|}{\max(M^*) - \min(M^*)} \tag{2.47}$$

where $M_{i,j}$ is the term at the i^{th} line j^{th} column of $[\mathbf{M}]$ and M^* are all the non diagonal terms of $[\mathbf{M}]$. Note that we consider only the real part of each term. The W factor for inductance matrices presented Tab. A.15 to A.26 all exceeds 99 %. In comparison, the expected W factor is about $60.6\,\%^{+10.2\,\%}_{-10.6\,\%}$ for a random 4×4 matrix and $64.4\,\%^{+6.1\,\%}_{-6.4\,\%}$ for a 6×6 one. Model and experiments are consistent on this point.

2.4.2 Inductance

Based on Lenz's Law, the self inductance of a simple conductor is always positive. At 15 MHz both PCB and rotary array's self-inductance are negative (Cf. diagonal terms of the inductance matrices Tables A.15 to A.26). On the other hand, we can observe an unusually large imaginary part at low
frequency.

Stray capacitance may intuitively explain the negative self-inductance at high frequency. On the large imaginary part issue, we must acknowledge that an inductance's imaginary part is homogeneous to the real part of a complex impedance, i.e., a resistance. Indeed, the issue lies in the poor conditioning of the matrix [**M**] with respect to the ESR matrix [**R**] at low frequency.

Using a SPICE program to simulate the behavior of a simplified version of the PCB array experimental setup (Cf. Fig. 2.14), we observed that the $\pm 0.01\,\Omega$ measurement tolerance on [**R**] corresponds to about $\pm 10\,\mu H$ deviation on the calculated self-inductance's imaginary part. In the mean time, we also noticed that even 90 pF per probe + oscilloscope input capacitance (very conservative value considering that we used straight 1.2 m unterminated lossless coaxial cables) is enough to significantly bias the calculated value of [**M**] above 3 MHz (Cf. Fig. 2.15). Hence the negative values obtained at 15 MHz.

Notice that however a negative self-inductance might be alarming, negative mutual inductance isn't. The observed negative co-channel mutual inductance $M_{B2,T2}$ is consistent over the whole test frequency range. Indeed, this simply denotes that either ζ_{B2} or ζ_{T2} was plugged in reverse polarity.

2.4.3 Coupling and Selectivity

In the numerical analysis Section 2.3.1, we would expect the ACRR of the PCB array to tend to infinity at position $(0, 0, 1)_{O;\hat{\mathbf{i}},\hat{\mathbf{j}},\hat{\mathbf{k}}}$ between every channels. Instead we observed filtering capabilities globally lower than 100 dB at that position. Furthermore, the highest filtering position varies from channel to channel.

Indeed, unlike the simple loop geometry used in example 2.1.2, the spiral geometry used here is not perfectly symmetric. To a smaller extend this might be due to

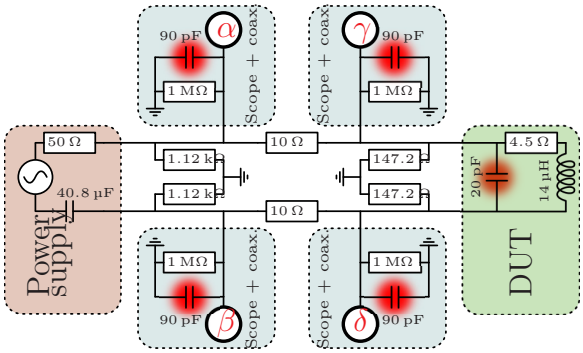

Figure 2.14: Schematic of the portion of the tested circuit simulated with the software ngspice-26. Parasitic capacitance are highlighted with blurry red dots. Scope inputs α, β, γ and δ are that presented in Fig. 2.8. Results of the simulation are presented Fig. 2.15.

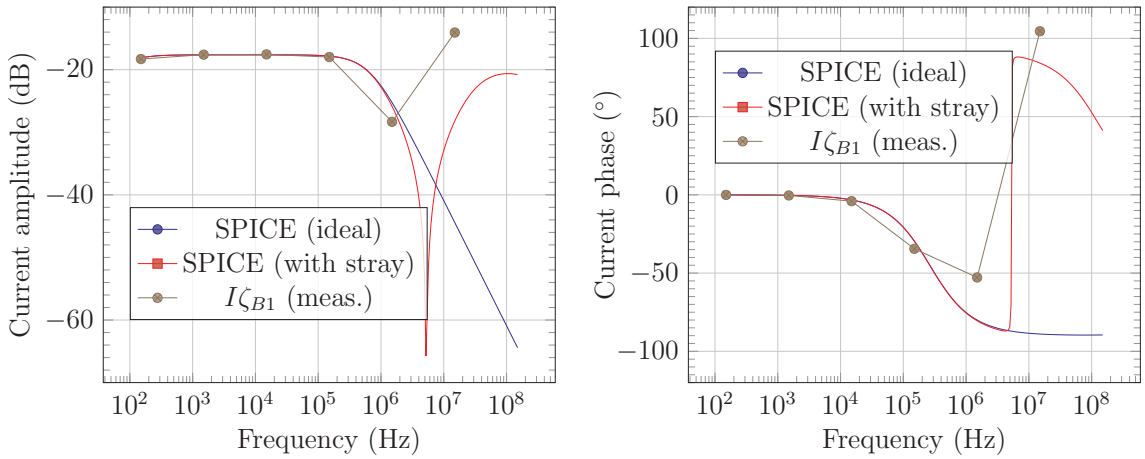

Figure 2.15: Comparison of the signal $(294.4 \times \Delta\alpha\beta - 314.4\Delta\gamma\delta)/5888$ between the simulated circuit Fig. 2.14 and the real antenna ζ_{B1}. The result allows to estimate the resonance frequency, above which the capacitive impedance will dominate over the inductance of a 14 µF antenna, thus leading to wrong calculation of the self inductance with our method (negative values). This is put in perspective with an ideal situation where the circuit would not contain parasitic capacitance. Their is not enough measurement points to precisely determine the resonance frequency of the real device. However, the curve obtained from simulation fits well enough the measurements to conclude that at 15 MHz the system definitely operates above its resonance frequency.

the numerical bias introduced by numerical round-off and the limited resolution of the numerical model.

The ACRR of the experimental rotary array is substantial over the whole tested frequency range: above 20 dB. However, it is about 3 orders of magnitude lower than

the expected values from numerical evaluation.

It is reasonable to think that this high discrepancy is mainly due to the relatively poor building accuracy of the experimental device (machined with a drill press) and of the acquisition system. As can be seen on Fig. 2.12 a misalignment of only 0.1 mm could account for this difference. This might be further emphasize by the low number of turns (higher sensitivity to random error) and by the compactness of the system in comparison to the PCB array.

Based on its definition (Equations (2.43) and (2.42)), ACRR's should be independent of the operating frequency. For both experimental devices, the calculated absolute ratio between co-channel and cross-channel coupling is higher than 10 (20 dB of ACRR) up to 1.5 MHz. Above that frequency, the ratio collapses to as low as 1.7 (about 5 dB). This phenomenon was not predicted by the presented Pie-Chart antenna model.

It is tempting to think that this is another consequence of the stray mutual capacitance between channels. Yet, given how randomly affected each ACRR seemed to be (at 15 MHz $\mathcal{S}_{3,1} \simeq 10\,\text{dB}$ whereas $\mathcal{S}_{2,3} \simeq 40\,\text{dB}$) we would expect an equally random capacitive coupling matrix for the system. Considering how similar we tried to make each antenna of the PCB device (similar self-inductance, similar total wire length hence the similar antenna ESR seen Table A.1, similar copper trace surface area) and the fact that each pair of wire were twisted, we would not expect the capacitance matrix of the system to be random. Similarly, explaining the sudden increase of $\mathcal{S}_{D,P}$ of the rotary array might be a not-so-obvious task.

Chapter 3

Refined Model

"*Essentially, all models are wrong, but some are useful* [22]"

In our previous model, we concluded that the low cross-channel mutual inductance accounts for the very high theoretical ACRR of pie-chart configuration. However, as mutual inductance has no tangible reality at high frequencies, our previous approach using Neumann's equation leads to incomplete or misleading conclusion when signal wavelength is of the same order of magnitude as the cord length of a pie-chart array. In this chapter we will refine our model using progressively more accurate laws of Classical ElectroMagnetics, thus naturally pointing out specificities of the Pie-Chart Antenna concept.

3.1 Quasi-static magnetism: Biot-Savart approach

As long as the signal wavelength is orders of magnitude higher than the antenna's chord, the magnetostatic approximation often comes in handy for simplifying magnetic induction analysis. But as the wavelength get closer to antenna's chord length (quasi static current state), "strange" phenomenon arise which could eventually lead to significantly reduce the crosstalk suppression capabilities of a Pie-Chart array if build as described earlier.

We will consider the exact same configuration as described previously. However, in this subsection we will not directly use the mutual inductance but instead the magnetic flux to highlight one specificity of the Pie-Chart concept.

In that regard, we remind here the relation between the magnetic flux and the mutual inductance:

$$\Phi_{i,j} = M_{i,j} \cdot i_i \tag{3.1}$$

where $\Phi_{i,j}$ is the flux of the magnetic field $\vec{B}_{i,j}$ generated by the current i_i flowing through ζ_i into the surface S_j bordered by the closed loop ζ_j.

Lets introduce the ruled open surfaces S_i defined by the collection of segments $[A, \zeta_i(\gamma)]$. A point N_i of S_i is defined by $\overrightarrow{AN}_i(\gamma, \delta) = \delta \cdot \overrightarrow{A\zeta}_i(\gamma)$ with $\delta \in [0; 1]$. A small element of S_i is:

$$\overrightarrow{dS}_i(\gamma, \delta) = (\ d\delta \cdot \overrightarrow{A\zeta}_i(\gamma)\ ) \times (\ \delta \cdot \vec{dl}_i(\gamma)\ ) \tag{3.2}$$

The magnetic flux $\Phi_{i,j}$ from the magnetic field $\vec{B}_{i,j}(\vec{N}_i(\gamma, \delta))$ generated by the current $\vec{i}_i$ flowing through each point $\zeta_i(\gamma)$ into each element $dS_j(\gamma, \delta)$ of S_j is expressed as:

$$\Phi_{i,j} = \int_{S_j} \vec{B}_{i,j}(\vec{N}_j) \cdot \overrightarrow{dS}_j \tag{3.3}$$

Focusing on the arrays ζ_E and ζ_F, we can write the following:

$$\Phi_{E_i F_k} = \int_{\delta=0}^{1} \delta \cdot [\int_{\zeta_{F_k}} \vec{B}_{E_i,F_k} \cdot (\ \overrightarrow{A\zeta}_{F_k} \times \vec{dl}_{F_k}\ )] \cdot d\delta \tag{3.4}$$

with $\vec{dl}_{F_k} = \frac{\vec{\zeta}'_{F_k}}{\|\vec{\zeta}'_{F_k}\|} \cdot d\alpha$. Based on Biot-Savart law, the magnetic field $\vec{B}_{E_i,F_k}(\vec{N}_{F_k}(\gamma, \delta))$ is known as:

$$\vec{B}_{E_i,F_k}(\vec{N}_{F_k}(\gamma, \delta)) = \frac{\mu_0}{4\pi} \int_{-e}^{e} \frac{\vec{i}_{E_i}(\alpha) \times \vec{r}_{F_k E_i}(\gamma, \alpha, \delta)}{\|\vec{r}_{F_k E_i}(\gamma, \alpha, \delta)\|^3}\, d\alpha \tag{3.5}$$

where $\vec{r}_{F_k E_i}(\gamma, \alpha, \delta) = \vec{N}_{F_k}(\gamma, \delta) - \vec{\zeta}_{E_i}(\alpha)$. Taking notice that $\zeta_{E_j}(\alpha) = \overset{\vec{n},\vec{A}}{\rightleftharpoons} \zeta_{E_i}(-\alpha)$ and $\vec{N}_{F_l}(\gamma, \delta) = Z(N_{F_k}(\gamma, \delta), \vec{n}, \vec{A})$ then carrying the necessary algebra, we establish for every point $N_{F_k}(\gamma, \delta)$ of S_{F_k} and $N_{F_l}(\gamma, \delta)$ of S_{F_l}:

$$\vec{B}_{E_j,F_l} = \frac{i_{E_j}}{i_{E_i}} \frac{1}{\vec{n}^2}\ [\mathbf{C}]\ \frac{\mu_0}{4\pi} \times \int_{-e}^{e} \frac{\vec{i}_{E_i}(-\alpha) \times \vec{r}_{F_k E_i}(\gamma, -\alpha, \delta)}{\|\vec{r}_{F_k E_i}(\gamma, -\alpha, \delta)\|^3}\, d\alpha$$

$$\vec{B}_{E_j,F_l}(\vec{N}_{F_l}(\gamma, \delta)) = \frac{i_{E_j}}{i_{E_i}} \overset{\vec{n},\vec{0}}{\widetilde{B}}_{E_i,F_k}(\ \vec{N}_{F_k}(\gamma, \delta)\ ) \tag{3.6}$$

Injecting (3.6) into (3.4), we get:

$$\Phi_{E_j,F_l} = \int_{\delta=0}^{1} \delta \cdot [\int_{\zeta_{F_l}} \frac{i_{E_j}}{i_{E_i}} \overset{\vec{n},\vec{0}}{\widetilde{B}}_{E_i,F_k} \cdot \underbrace{(\ \overset{\vec{n},\vec{0}}{\widetilde{A\zeta}}_{F_k} \times \overset{\vec{n},\vec{0}}{\widetilde{dl}}_{F_k}\ )}_{-\overrightarrow{A\zeta}_{F_k} \times \vec{dl}_{F_k}}] \cdot d\delta \tag{3.7}$$

Thus resulting in[1]:

$$\Phi_{E_j,F_l} = -\frac{i_{E_j}}{i_{E_i}}\,\Phi_{E_i,F_k} \tag{3.8}$$

Proceeding similarly for every couple of array, reaching the partial conclusion 2.1.2 is straightforward.

Here however, this approach using Biot-Savart law reveals that the control of the currents symmetry/anti-symmetry through antennas of a pie array is of utmost importance. From a practical point of view, improper control could result in signal distortion or poor crosstalk suppression capabilities. Fortunately, proper operation can usually be achieved at high frequency using careful symmetric design and balanced current feed.

3.2 Magnetodynamic: Faraday's filamentary loop

At high frequency current can no longer be considered uniform along the antenna path and the magnetic field has a propagation pattern influenced by relativistic effects. To deals we some specificities of the field at those frequencies, we propose to refine the Pie-Chart antenna model using the Jeffimenko's equation [23] for the B-field at retarded time between closed static filamentary antennas[2]:

$$\vec{B}_{E_j,F_l}(\vec{N}_{F_l}(\gamma,\delta),t) = \frac{\mu_0}{4\pi}\Big(\overbrace{\int_{-e}^{e}\frac{\vec{i}_{E_j}(\alpha,\tau)\times\vec{r}_{F_l,E_j}(\gamma,\alpha,\delta)}{\|\vec{r}_{F_l,E_j}(\gamma,\alpha,\delta)\|^3}\,d\alpha}^{B1} + \underbrace{\int_{-e}^{e}\frac{\dot{\vec{i}}_{E_j}(\alpha,\tau)\times\vec{r}_{F_l,E_j}(\gamma,\alpha,\delta)}{c\|\vec{r}_{F_l,E_j}(\gamma,\alpha,\delta)\|^2}\,d\alpha}_{B2}\Big) \tag{3.9}$$

where $\tau = t - \|\vec{r}_{F_kE_i}\|/c = t - \|\vec{r}_{F_lE_j}\|/c$ with t being the time for which $\vec{B}_{E_i,F_k}$ is evaluated.

Now lets assume that currents are no longer symmetric (or anti-symmetric) within

[1] this result is true whatever the chosen definition of the open surfaces S_m if bordered by the contour ζ_m and oriented by $\vec{dl}_m$ because of the conservative nature of the magnetic flux

[2] We chose the filamentary approximation for the only sake of simplicity. The same conclusion is reachable using the volumetric integration of the current density J.

the arrays, but that their first order time derivative are. This can be written as:

$$\forall i \leq m \ : \ \dot{\vec{i}}_{E_i}(\alpha, t) \ = \ -\dot{\vec{i}}_{E_j}(-\alpha, t) \tag{3.10}$$

$$\forall i \leq n \ : \ \dot{\vec{i}}_{F_i}(\alpha, t) \ = \ \dot{\vec{i}}_{F_j}(\alpha, t) \tag{3.11}$$

Thus giving:

$$\forall i \leq m \ : \ \vec{i}_{E_j}(\alpha, t) \ = \ (W - i_{E_i}(-\alpha, t)) \cdot \hat{\mathbf{i}}_{E_i}(-\alpha) \tag{3.12}$$

$$\forall i \leq n \ : \ \vec{i}_{F_j}(\alpha, t) \ = \ (X + i_{F_i}(\alpha, t)) \cdot \hat{\mathbf{i}}_{F_i}(\alpha) \tag{3.13}$$

where W and X are some arbitrary constants. Therefore, if every arrays maintain their symmetry or anti-symmetry over time:

$$B1(t) \ = \ \frac{1}{\vec{n}^2} \ [\mathbf{C}] \times \Big(\int_{-e}^{e} \frac{\vec{i}_{E_i}(-\alpha, \tau) \times \vec{r}_{F_k E_i}(\gamma, -\alpha, \delta)}{\|\vec{r}_{F_k E_i}(\gamma, -\alpha, \delta)\|^3} \, d\alpha + \underbrace{W \int_{-e}^{e} \frac{\hat{\mathbf{i}}_{E_i}(-\alpha) \times \vec{r}_{F_k E_i}(\gamma, -\alpha, \delta)}{\|\vec{r}_{F_k E_i}(\gamma, -\alpha, \delta)\|^3} \, d\alpha}_{\mathcal{F}(\gamma, \delta)} \Big) \tag{3.14}$$

and:

$$B2(t) \ = \ \frac{1}{\vec{n}^2} \ [\mathbf{C}] \times \int_{-e}^{e} \frac{\dot{\vec{i}}_{E_i}(-\alpha, \tau) \times \vec{r}_{F_k E_i}(\gamma, -\alpha, \delta)}{\|\vec{r}_{F_k E_i}(\gamma, -\alpha, \delta)\|^3} \, d\alpha \tag{3.15}$$

which results in:

$$\vec{B}_{E_j, F_l}(\vec{N}_{F_l}(\gamma, \delta), t) \ = \ \overset{\vec{n}, \vec{0}}{\widetilde{B}}_{E_i, F_k}(\vec{N}_{F_l}(\gamma, \delta), t) + \overset{\vec{n}, \vec{0}}{\widetilde{\mathcal{F}}}(\gamma, \delta) \tag{3.16}$$

$$\Rightarrow \ \frac{d \ \vec{B}_{E_j, F_l}(\vec{N}_{F_l}(\gamma, \delta), t)}{dt} \ = \ \frac{d \ \overset{\vec{n}, \vec{0}}{\widetilde{B}}_{E_i, F_k}(\vec{N}_{F_l}(\gamma, \delta), t)}{dt} \tag{3.17}$$

We remind here that the EMF $\Delta V_j(i_i)$ across the terminal of an inductor ζ_j induced by the current of time varying intensity $i_i(t)$ flowing through an antenna ζ_i can be determined at any instant t using the bellow expression of Faraday's law of induction:

$$\Delta V_j(i_i(t)) = \frac{d \ \Phi_{i,j}(t)}{dt} \tag{3.18}$$

Therefore the above equation (3.17) leads to:

$$\Delta V_{F_l}(i_{E_j}) = \frac{d \ \Phi_{E_j, F_l}}{dt} = -\frac{d \ \Phi_{E_i, F_k}}{dt} = -\Delta V_{F_k}(i_{E_i}) \tag{3.19}$$

Similarly, we can establish that:

$(i,k) \in \mathbb{N}^{2*}$:

$$\forall (i,k) \leq (n,o) \ : \ \Delta V_{F_i}(i_{G_k}) = -\Delta V_{F_j}(i_{G_l}) \tag{3.20}$$

$$\forall (i,k) \leq (m,p) \ : \ \Delta V_{E_i}(i_{H_k}) = -\Delta V_{E_j}(i_{H_l}) \tag{3.21}$$

$$\forall (i,k) \leq (o,p) \ : \ \Delta V_{G_i}(i_{H_k}) = -\Delta V_{G_j}(i_{H_l}) \tag{3.22}$$

$$\forall (i,k) \leq (m,o) \ : \ \Delta V_{E_i}(i_{G_k}) = \Delta V_{E_j}(i_{G_l}) \tag{3.23}$$

$$\forall (i,k) \leq (n,p) \ : \ \Delta V_{F_i}(i_{H_k}) = \Delta V_{F_j}(i_{H_l}) \tag{3.24}$$

providing that:

$$\forall i \leq o \ : \ \dot{\vec{i}}_{G_i}(\alpha,t) \ = \ -\dot{\vec{i}}_{G_j}(-\alpha,t) \tag{3.25}$$

$$\forall i \leq p \ : \ \dot{\vec{i}}_{H_i}(\alpha,t) \ = \ \dot{\vec{i}}_{H_j}(\alpha,t) \tag{3.26}$$

From this point again, reaching the partial conclusion 2.1.2 is straightforward.

However, the one important point about the presented approach is that equations (3.14) and (3.15) were obtained under the strict assumption of the preserved symmetry and anti-symmetry of the currents' first order derivative at every instant in time within emitting arrays. From a practical point of view, this means that DC bias currents can be supplied to any antenna without altering co-channel coupling or crosstalk suppression capabilities.

Chapter 4

Conclusion

A specific topology of multichannel inductive array of antennas was presented. It was shown to be theoretically efficient in filtering crosstalk. That was experimentally confirmed over a 150 Hz $\sim$ 1.5 MHz frequency range. Building process, based on iterative symmetries, allows for very quick and cheap yet efficient design and manufacturing of multichannel device. This design simplicity was especially exemplified with the quick build and test of the 2 channels rotary type of inductive transmission device (wireless "slip ring").

Yet, we were unable to prove the effectiveness of the concept above this frequency range because of a too high amount of stray capacitance in the test system and because of an unexpected incoherent drop of ACRR at high frequency. Further investigations on those issues are currently carried for a more complete understanding of the physics at play.

Appendix A

Detailed experimental results

Table A.1: Calculated and measured Equivalent Series Resistance R_i (PCB array)

	R_{B1}	R_{B2}	R_{B3}	R_{T1}	R_{T2}	R_{T3}
Calculated (Ω)	4.38	4.81	5.13	4.38	4.81	5.13
Measured (Ω)	4.48	4.77	5.01	4.67	4.72	5.03
Error (%)	2.5	0.7	2.4	6.6	1.7	1.9

Table A.2: Calculated and measured Equivalent Series Resistance R_i (rotary array)

	R_{Pin}	R_{Din}	R_{Pout}	R_{Dout}
Calculated (Ω)	0.50	0.22	0.46	0.20
Measured (Ω)	0.52	0.16	0.45	0.23
Error (%)	3	28	3	13

Table A.3: Current through the inductors evaluated at 150 Hz (rotary array)

(mA)	XP_1	XP_2	XP_3	XP_4
$I\zeta_{Pin}$	129.12 $-0.05°$	0.00 $64.95°$	0.01 $-90.13°$	0.00 $131.20°$
$I\zeta_{Din}$	0.00 $87.32°$	129.82 $-0.01°$	0.00 $84.04°$	0.00 $90.55°$
$I\zeta_{Pout}$	0.01 $-90.14°$	0.00 $96.99°$	129.22 $-0.05°$	0.00 $-71.59°$
$I\zeta_{Dout}$	0.00 $-60.46°$	0.00 $89.37°$	0.00 $-78.92°$	129.71 $-0.00°$

Table A.4: Current through the inductors evaluated at 1.5 kHz (rotary array)

(mA)	XP_1	XP_2	XP_3	XP_4
$I\zeta_{Pin}$	140.70 $-0.53°$	0.00 $88.43°$	0.06 $-90.62°$	0.00 $-139.11°$
$I\zeta_{Din}$	0.00 $87.41°$	141.63 $-0.06°$	0.00 $88.48°$	0.00 $89.85°$
$I\zeta_{Pout}$	0.06 $-90.67°$	0.00 $91.15°$	140.91 $-0.48°$	0.00 $-90.02°$
$I\zeta_{Dout}$	0.00 $-88.52°$	0.00 $89.73°$	0.00 $-90.41°$	141.44 $-0.05°$

Table A.5: Current through the inductors evaluated at 15 kHz (rotary array)

(mA)	XP_1	XP_2	XP_3	XP_4
$I\zeta_{Pin}$	141.29 $-5.33°$	0.00 $89.48°$	0.61 $-95.28°$	0.00 $166.05°$
$I\zeta_{Din}$	0.00 $84.47°$	142.25 $-0.56°$	0.00 $84.82°$	0.04 $89.35°$
$I\zeta_{Pout}$	0.61 $-95.74°$	0.00 $89.19°$	141.43 $-4.85°$	0.00 $-91.29°$
$I\zeta_{Dout}$	0.00 $80.15°$	0.04 $89.32°$	0.00 $-94.23°$	142.05 $-0.53°$

Table A.6: Current through the inductors evaluated at 150 kHz (rotary array)

(mA)	XP_1	XP_2	XP_3	XP_4
$I\zeta_{Pin}$	133.35 $-41.55°$	0.01 $77.03°$	5.79 $-133.17°$	0.00 $174.37°$
$I\zeta_{Din}$	0.01 $44.62°$	141.31 $-5.52°$	0.03 $48.92°$	0.38 $83.84°$
$I\zeta_{Pout}$	5.75 $-135.47°$	0.03 $79.98°$	134.46 $-39.01°$	0.02 $-100.01°$
$I\zeta_{Dout}$	0.00 $124.15°$	0.38 $83.55°$	0.01 $-130.52°$	141.13 $-5.18°$

Table A.7: Current through the inductors evaluated at 1.5 MHz (rotary array)

(mA)	XP_1	XP_2	XP_3	XP_4
$I\zeta_{Pin}$	37.77 $-59.39°$	0.10 $-15.46°$	18.30 $171.32°$	0.08 $95.55°$
$I\zeta_{Din}$	0.04 $-4.43°$	133.47 $-41.80°$	0.09 $12.73°$	3.58 $44.29°$
$I\zeta_{Pout}$	17.12 $172.33°$	0.23 $15.00°$	41.59 $-58.09°$	0.14 $-173.44°$
$I\zeta_{Dout}$	0.03 $96.83°$	3.57 $43.00°$	0.06 $-173.03°$	134.14 $-40.02°$

Table A.8: Current through the inductors evaluated at 15 MHz (rotary array)

(mA)	XP_1	XP_2	XP_3	XP_4
$I\zeta_{Pin}$	198.55 109.43°	0.11 104.76°	3.21 17.84°	0.15 −24.53°
$I\zeta_{Din}$	0.18 99.15°	126.64 118.17°	0.32 −178.64°	15.89 −140.40°
$I\zeta_{Pout}$	3.19 18.22°	0.24 −179.13°	188.70 106.11°	0.40 15.19°
$I\zeta_{Dout}$	0.30 −2.90°	17.19 −137.41°	0.74 25.57°	115.89 115.65°

Table A.9: Current through the inductors evaluated at 150 Hz (PCB array)

(mA)	XP_1	XP_2	XP_3	XP_4	XP_5	XP_6
$I\zeta_{B1}$	121.66 −0.04°	0.00 67.99°	0.00 −134.34°	0.01 −90.10°	0.00 29.72°	0.00 3.64°
$I\zeta_{B2}$	0.00 31.01°	121.07 −0.04°	0.00 175.45°	0.00 25.98°	0.01 89.88°	0.00 −90.19°
$I\zeta_{B3}$	0.00 −23.31°	0.00 113.23°	120.65 −0.04°	0.00 14.07°	0.00 −46.67°	0.01 −90.08°
$I\zeta_{T1}$	0.01 −90.08°	0.00 83.31°	0.00 94.08°	121.23 −0.04°	0.00 68.65°	0.00 63.99°
$I\zeta_{T2}$	0.00 105.42°	0.01 89.94°	0.00 −96.83°	0.00 171.64°	121.17 −0.04°	0.00 −172.91°
$I\zeta_{T3}$	0.00 40.67°	0.00 −126.74°	0.01 −90.05°	0.00 64.59°	0.00 −22.46°	120.57 −0.04°

Table A.10: Current through the inductors evaluated at 1.5 kHz (PCB array)

(mA)	XP_1	XP_2	XP_3	XP_4	XP_5	XP_6
$I\zeta_{B1}$	131.83 $-0.38°$	0.00 $85.74°$	0.00 $86.10°$	0.06 $-90.52°$	0.00 $84.50°$	0.00 $83.55°$
$I\zeta_{B2}$	0.00 $91.49°$	131.18 $-0.38°$	0.00 $92.85°$	0.00 $86.85°$	0.06 $89.46°$	0.00 $-99.30°$
$I\zeta_{B3}$	0.00 $83.11°$	0.00 $77.45°$	130.62 $-0.38°$	0.00 $87.63°$	0.00 $-91.89°$	0.06 $-90.53°$
$I\zeta_{T1}$	0.06 $-90.54°$	0.00 $88.76°$	0.00 $95.11°$	131.36 $-0.38°$	0.00 $77.99°$	0.00 $80.66°$
$I\zeta_{T2}$	0.00 $90.54°$	0.06 $89.46°$	0.00 $-89.31°$	0.00 $90.95°$	131.22 $-0.38°$	0.00 $-123.75°$
$I\zeta_{T3}$	0.00 $85.50°$	0.00 $-92.06°$	0.06 $-90.54°$	0.00 $86.03°$	0.00 $-146.17°$	130.58 $-0.38°$

Table A.11: Current through the inductors evaluated at 15 kHz (PCB array)

(mA)	XP_1	XP_2	XP_3	XP_4	XP_5	XP_6
$I\zeta_{B1}$	132.41 $-4.03°$	0.00 $85.08°$	0.00 $84.29°$	0.61 $-94.45°$	0.00 $87.22°$	0.00 $84.17°$
$I\zeta_{B2}$	0.00 $82.52°$	131.75 $-4.03°$	0.00 $79.27°$	0.00 $82.46°$	0.60 $85.50°$	0.00 $-92.24°$
$I\zeta_{B3}$	0.00 $76.24°$	0.00 $81.22°$	131.21 $-3.99°$	0.00 $80.05°$	0.00 $-93.24°$	0.58 $-94.47°$
$I\zeta_{T1}$	0.61 $-94.48°$	0.00 $85.36°$	0.00 $84.04°$	131.92 $-4.00°$	0.00 $85.75°$	0.00 $83.37°$
$I\zeta_{T2}$	0.00 $80.82°$	0.60 $85.51°$	0.00 $-92.56°$	0.00 $79.98°$	131.78 $-4.03°$	0.00 $-82.99°$
$I\zeta_{T3}$	0.00 $78.87°$	0.00 $-91.57°$	0.58 $-94.47°$	0.00 $80.69°$	0.00 $-82.39°$	131.10 $-3.98°$

Table A.12: Current through the inductors evaluated at 150 kHz (PCB array)

(mA)	XP_1	XP_2	XP_3	XP_4	XP_5	XP_6
$I\zeta_{B1}$	126.18 $-34.47°$	0.00 $50.76°$	0.00 $60.41°$	5.77 $-128.19°$	0.00 $61.81°$	0.00 $52.90°$
$I\zeta_{B2}$	0.00 $55.99°$	125.40 $-34.48°$	0.00 $50.68°$	0.00 $55.77°$	5.75 $51.45°$	0.00 $-130.58°$
$I\zeta_{B3}$	0.00 $65.73°$	0.00 $53.39°$	124.92 $-34.23°$	0.00 $49.34°$	0.01 $-131.49°$	5.47 $-128.32°$
$I\zeta_{T1}$	5.72 $-128.39°$	0.00 $58.87°$	0.00 $63.55°$	125.71 $-34.27°$	0.00 $83.34°$	0.00 $57.68°$
$I\zeta_{T2}$	0.00 $57.63°$	5.69 $51.51°$	0.01 $-131.57°$	0.00 $59.52°$	125.45 $-34.48°$	0.00 $-141.09°$
$I\zeta_{T3}$	0.00 $50.75°$	0.00 $-130.01°$	5.47 $-128.38°$	0.00 $49.21°$	0.00 $-141.29°$	124.86 $-34.10°$

Table A.13: Current through the inductors evaluated at 1.5 MHz (PCB array)

(mA)	XP_1	XP_2	XP_3	XP_4	XP_5	XP_6
$I\zeta_{B1}$	38.34 $-52.80°$	0.11 $-58.33°$	0.03 $-38.38°$	18.70 $175.88°$	0.04 $88.63°$	0.02 $11.29°$
$I\zeta_{B2}$	0.03 $90.52°$	38.21 $-52.84°$	0.02 $104.15°$	0.03 $85.94°$	18.51 $-4.76°$	0.05 $124.61°$
$I\zeta_{B3}$	0.03 $102.30°$	0.03 $108.77°$	39.29 $-55.74°$	0.03 $86.78°$	0.04 $130.94°$	17.93 $174.06°$
$I\zeta_{T1}$	18.75 $175.83°$	0.01 $42.26°$	0.06 $103.37°$	38.21 $-52.82°$	0.16 $109.62°$	0.08 $103.78°$
$I\zeta_{T2}$	0.03 $101.83°$	18.43 $-4.73°$	0.05 $122.09°$	0.04 $104.32°$	38.50 $-52.56°$	0.03 $109.32°$
$I\zeta_{T3}$	0.04 $108.18°$	0.05 $127.96°$	17.82 $174.06°$	0.04 $101.02°$	0.04 $112.68°$	39.25 $-54.54°$

Table A.14: Current through the inductors evaluated at 15 MHz (PCB array)

(mA)	XP_1	XP_2	XP_3	XP_4	XP_5	XP_6
$I\zeta_{B1}$	198.25 $104.56°$	0.07 $92.68°$	0.31 $138.54°$	6.02 $13.80°$	0.09 $8.76°$	0.57 $6.10°$
$I\zeta_{B2}$	0.08 $66.82°$	183.01 $104.31°$	0.10 $8.02°$	0.08 $76.93°$	5.87 $-164.94°$	0.06 $57.71°$
$I\zeta_{B3}$	0.37 $140.20°$	0.03 $23.34°$	194.39 $104.98°$	0.54 $172.09°$	0.06 $52.31°$	1.97 $23.38°$
$I\zeta_{T1}$	6.01 $15.39°$	0.12 $112.53°$	0.56 $175.93°$	186.25 $101.77°$	0.12 $35.02°$	0.31 $11.85°$
$I\zeta_{T2}$	0.07 $40.07°$	5.53 $-163.50°$	0.06 $77.61°$	0.08 $37.55°$	198.82 $101.71°$	0.07 $122.07°$
$I\zeta_{T3}$	0.47 $1.79°$	0.06 $49.38°$	1.90 $23.86°$	0.35 $1.00°$	0.07 $141.85°$	206.94 $103.98°$

Table A.15: Evaluated PCB array's inductance matrix at 150 Hz[1]

(µH)	$M_{B1,j}$	$M_{B2,j}$	$M_{B3,j}$	$M_{T1,j}$	$M_{T2,j}$	$M_{T3,j}$
$M_{i,B1}$	16.540 $-96.211\jmath$	-0.010 $+0.004\jmath$	0.003 $-0.003\jmath$	14.283 $-0.016\jmath$	-0.011 $+0.019\jmath$	-0.001 $+0.015\jmath$
$M_{i,B2}$	-0.004 $+0.007\jmath$	17.119 $+39.142\jmath$	-0.002 $-0.021\jmath$	-0.002 $+0.004\jmath$	-14.303 $+0.020\jmath$	0.007 $-0.000\jmath$
$M_{i,B3}$	0.001 $+0.003\jmath$	-0.011 $-0.005\jmath$	17.795 $+121.928\jmath$	-0.005 $+0.020\jmath$	0.009 $+0.009\jmath$	13.835 $-0.010\jmath$
$M_{i,T1}$	14.298 $-0.008\jmath$	-0.014 $+0.002\jmath$	-0.023 $-0.002\jmath$	16.685 $-307.465\jmath$	-0.008 $+0.003\jmath$	-0.013 $+0.006\jmath$
$M_{i,T2}$	-0.014 $-0.004\jmath$	-14.299 $+0.005\jmath$	0.023 $-0.003\jmath$	-0.002 $-0.015\jmath$	16.457 $+80.503\jmath$	0.003 $-0.023\jmath$
$M_{i,T3}$	-0.007 $+0.008\jmath$	0.012 $-0.009\jmath$	13.842 $-0.002\jmath$	-0.013 $+0.006\jmath$	0.008 $+0.019\jmath$	16.440 $+89.336\jmath$

[1]Notice that the real part is the actual inductance whereas the imaginary part is homogeneous to a resistance.

Table A.16: Evaluated PCB array's inductance matrix at 1.5 kHz[1]

(µH)	$M_{B1,j}$	$M_{B2,j}$	$M_{B3,j}$	$M_{T1,j}$	$M_{T2,j}$	$M_{T3,j}$
$M_{i,B1}$	16.499 $-9.046\jmath$	-0.008 $+0.001\jmath$	-0.003 $+0.000\jmath$	14.559 $-0.029\jmath$	-0.005 $+0.000\jmath$	-0.008 $+0.001\jmath$
$M_{i,B2}$	-0.010 $-0.000\jmath$	16.659 $+4.786\jmath$	-0.006 $-0.000\jmath$	-0.010 $+0.000\jmath$	-14.567 $+0.032\jmath$	0.007 $-0.001\jmath$
$M_{i,B3}$	-0.003 $+0.000\jmath$	-0.005 $+0.001\jmath$	16.635 $+13.168\jmath$	-0.006 $+0.000\jmath$	0.012 $-0.000\jmath$	14.084 $-0.032\jmath$
$M_{i,T1}$	14.558 $-0.033\jmath$	-0.009 $+0.000\jmath$	-0.006 $-0.001\jmath$	16.430 $-29.744\jmath$	-0.004 $+0.001\jmath$	-0.008 $+0.001\jmath$
$M_{i,T2}$	-0.008 $-0.000\jmath$	-14.569 $+0.033\jmath$	0.011 $+0.000\jmath$	-0.006 $-0.000\jmath$	16.619 $+9.185\jmath$	0.001 $-0.001\jmath$
$M_{i,T3}$	-0.007 $+0.000\jmath$	0.009 $-0.000\jmath$	14.089 $-0.031\jmath$	-0.009 $+0.001\jmath$	0.001 $-0.001\jmath$	16.525 $+10.095\jmath$

Table A.17: Evaluated PCB array's inductance matrix at 15 kHz[1]

(µH)	$M_{B1,j}$	$M_{B2,j}$	$M_{B3,j}$	$M_{T1,j}$	$M_{T2,j}$	$M_{T3,j}$
$M_{i,B1}$	17.324 $-0.813\jmath$	-0.009 $+0.000\jmath$	-0.003 $+0.000\jmath$	14.551 $-0.035\jmath$	-0.006 $-0.000\jmath$	-0.008 $+0.000\jmath$
$M_{i,B2}$	-0.010 $+0.001\jmath$	17.548 $+0.586\jmath$	-0.004 $+0.000\jmath$	-0.009 $+0.001\jmath$	-14.562 $+0.038\jmath$	0.008 $+0.000\jmath$
$M_{i,B3}$	-0.004 $+0.001\jmath$	-0.005 $+0.000\jmath$	17.569 $+1.425\jmath$	-0.006 $+0.001\jmath$	0.012 $+0.000\jmath$	14.082 $-0.043\jmath$
$M_{i,T1}$	14.551 $-0.035\jmath$	-0.008 $+0.000\jmath$	-0.005 $+0.000\jmath$	17.335 $-2.887\jmath$	-0.005 $+0.000\jmath$	-0.009 $+0.000\jmath$
$M_{i,T2}$	-0.007 $+0.001\jmath$	-14.559 $+0.037\jmath$	0.012 $+0.000\jmath$	-0.006 $+0.001\jmath$	17.540 $+1.008\jmath$	0.002 $+0.000\jmath$
$M_{i,T3}$	-0.006 $+0.001\jmath$	0.009 $+0.000\jmath$	14.083 $-0.040\jmath$	-0.008 $+0.001\jmath$	0.002 $+0.000\jmath$	17.519 $+1.094\jmath$

[1]Notice that the real part is the actual inductance whereas the imaginary part is homogeneous to a resistance.

Table A.18: Evaluated PCB array's inductance matrix at 150 kHz[1]

(µH)	$M_{B1,j}$	$M_{B2,j}$	$M_{B3,j}$	$M_{T1,j}$	$M_{T2,j}$	$M_{T3,j}$
$M_{i,B1}$	17.534 $-0.289\jmath$	-0.009 $+0.000\jmath$	-0.003 $-0.001\jmath$	14.578 $-0.192\jmath$	-0.006 $-0.001\jmath$	-0.007 $-0.000\jmath$
$M_{i,B2}$	-0.008 $-0.001\jmath$	17.776 $-0.168\jmath$	-0.003 $-0.000\jmath$	-0.008 $-0.001\jmath$	-14.581 $+0.221\jmath$	0.009 $-0.001\jmath$
$M_{i,B3}$	-0.002 $-0.001\jmath$	-0.003 $-0.000\jmath$	17.776 $-0.128\jmath$	-0.004 $-0.000\jmath$	0.014 $-0.001\jmath$	13.936 $-0.248\jmath$
$M_{i,T1}$	14.418 $-0.188\jmath$	-0.008 $-0.001\jmath$	-0.004 $-0.001\jmath$	17.556 $-0.509\jmath$	-0.003 $-0.002\jmath$	-0.007 $-0.001\jmath$
$M_{i,T2}$	-0.005 $-0.000\jmath$	-14.421 $+0.204\jmath$	0.014 $-0.001\jmath$	-0.004 $-0.000\jmath$	17.759 $-0.152\jmath$	0.003 $-0.001\jmath$
$M_{i,T3}$	-0.004 $-0.000\jmath$	0.011 $-0.001\jmath$	13.937 $-0.233\jmath$	-0.007 $-0.000\jmath$	0.003 $-0.001\jmath$	17.724 $-0.181\jmath$

Table A.19: Evaluated PCB array's inductance matrix at 1.5 MHz[1]

(µH)	$M_{B1,j}$	$M_{B2,j}$	$M_{B3,j}$	$M_{T1,j}$	$M_{T2,j}$	$M_{T3,j}$
$M_{i,B1}$	22.917 $-2.770\jmath$	-0.124 $+0.074\jmath$	0.015 $+0.008\jmath$	20.072 $-2.707\jmath$	0.136 $-0.062\jmath$	0.022 $-0.016\jmath$
$M_{i,B2}$	-0.007 $-0.041\jmath$	22.876 $-3.062\jmath$	-0.001 $-0.021\jmath$	-0.008 $-0.034\jmath$	-19.783 $+3.095\jmath$	0.019 $-0.042\jmath$
$M_{i,B3}$	0.049 $-0.041\jmath$	0.014 $-0.035\jmath$	21.938 $-2.536\jmath$	0.042 $-0.033\jmath$	0.023 $-0.033\jmath$	18.388 $-2.851\jmath$
$M_{i,T1}$	20.025 $-2.743\jmath$	-0.149 $+0.008\jmath$	0.049 $-0.076\jmath$	22.846 $-2.731\jmath$	0.112 $-0.128\jmath$	0.054 $-0.099\jmath$
$M_{i,T2}$	0.010 $-0.030\jmath$	-19.883 $+3.039\jmath$	0.034 $-0.048\jmath$	0.013 $-0.036\jmath$	22.829 $-3.138\jmath$	0.013 $-0.030\jmath$
$M_{i,T3}$	0.057 $-0.050\jmath$	0.029 $-0.043\jmath$	18.448 $-2.572\jmath$	0.049 $-0.045\jmath$	0.006 $-0.038\jmath$	21.921 $-2.942\jmath$

[1]Notice that the real part is the actual inductance whereas the imaginary part is homogeneous to a resistance.

Table A.20: Evaluated PCB array's inductance matrix at 15 MHz[1]

(µH)	$M_{B1,j}$	$M_{B2,j}$	$M_{B3,j}$	$M_{T1,j}$	$M_{T2,j}$	$M_{T3,j}$
$M_{i,B1}$	-0.560 $+0.393\jmath$	0.000 $+0.001\jmath$	-0.002 $+0.004\jmath$	0.090 $-0.015\jmath$	0.001 $-0.000\jmath$	0.007 $-0.002\jmath$
$M_{i,B2}$	0.001 $+0.001\jmath$	-0.609 $+0.408\jmath$	0.001 $-0.000\jmath$	0.001 $+0.001\jmath$	-0.083 $+0.013\jmath$	0.001 $+0.000\jmath$
$M_{i,B3}$	-0.002 $+0.005\jmath$	0.000 $-0.000\jmath$	-0.571 $+0.406\jmath$	-0.007 $+0.004\jmath$	0.001 $+0.000\jmath$	0.027 $-0.001\jmath$
$M_{i,T1}$	0.085 $-0.017\jmath$	0.000 $+0.002\jmath$	-0.007 $+0.004\jmath$	-0.602 $+0.374\jmath$	0.002 $+0.000\jmath$	0.004 $-0.001\jmath$
$M_{i,T2}$	0.001 $+0.000\jmath$	-0.085 $+0.014\jmath$	0.000 $+0.001\jmath$	0.001 $+0.000\jmath$	-0.565 $+0.369\jmath$	-0.000 $+0.001\jmath$
$M_{i,T3}$	0.006 $-0.003\jmath$	0.001 $+0.000\jmath$	0.028 $-0.001\jmath$	0.005 $-0.002\jmath$	-0.000 $+0.001\jmath$	-0.538 $+0.387\jmath$

Table A.21: Evaluated rotary array's inductance matrix at 150 Hz[1]

$M_{i,Pin}$	18.811 $-10.388\jmath$	-0.027 $+0.013\jmath$	13.279 $-0.017\jmath$	-0.002 $-0.002\jmath$
$M_{i,Din}$	-0.033 $+0.002\jmath$	1.918 $-9.111\jmath$	-0.067 $+0.007\jmath$	-0.828 $-0.008\jmath$
$M_{i,Pout}$	13.280 $-0.020\jmath$	-0.066 $-0.008\jmath$	17.008 $-10.514\jmath$	0.029 $+0.010\jmath$
$M_{i,Dout}$	0.013 $+0.007\jmath$	-0.819 $+0.009\jmath$	0.034 $+0.007\jmath$	1.728 $-11.318\jmath$

[1]Notice that the real part is the actual inductance whereas the imaginary part is homogeneous to a resistance.

Table A.22: Evaluated rotary array's inductance matrix at 1.5 kHz[1]

(µH)	$M_{Pin,j}$	$M_{Din,j}$	$M_{Pout,j}$	$M_{Dout,j}$
$M_{i,Pin}$	18.945 $-1.185\jmath$	-0.027 $+0.001\jmath$	13.529 $-0.024\jmath$	0.001 $-0.001\jmath$
$M_{i,Din}$	-0.030 $+0.001\jmath$	1.930 $-0.859\jmath$	-0.061 $+0.001\jmath$	-0.826 $+0.001\jmath$
$M_{i,Pout}$	13.532 $-0.025\jmath$	-0.059 $-0.001\jmath$	17.050 $-0.906\jmath$	0.035 $+0.000\jmath$
$M_{i,Dout}$	0.014 $+0.001\jmath$	-0.826 $+0.003\jmath$	0.032 $+0.000\jmath$	1.792 $-1.042\jmath$

Table A.23: Evaluated rotary array's inductance matrix at 15 kHz[1]

(µH)	$M_{Pin,j}$	$M_{Din,j}$	$M_{Pout,j}$	$M_{Dout,j}$
$M_{i,Pin}$	19.070 $-0.179\jmath$	-0.028 $-0.000\jmath$	13.524 $-0.020\jmath$	-0.000 $-0.000\jmath$
$M_{i,Din}$	-0.030 $-0.000\jmath$	1.973 $-0.083\jmath$	-0.061 $+0.000\jmath$	-0.835 $+0.001\jmath$
$M_{i,Pout}$	13.524 $-0.022\jmath$	-0.061 $-0.000\jmath$	17.286 $-0.164\jmath$	0.035 $-0.000\jmath$
$M_{i,Dout}$	-0.001 $+0.000\jmath$	-0.835 $+0.001\jmath$	0.033 $+0.000\jmath$	1.855 $-0.101\jmath$

[1]Notice that the real part is the actual inductance whereas the imaginary part is homogeneous to a resistance.

Table A.24: Evaluated rotary array's inductance matrix at 150 kHz[1]

(µH)	$M_{Pin,j}$	$M_{Din,j}$	$M_{Pout,j}$	$M_{Dout,j}$
$M_{i,Pin}$	18.946 $-0.328\jmath$	-0.029 $-0.001\jmath$	13.512 $-0.164\jmath$	0.000 $-0.000\jmath$
$M_{i,Din}$	-0.030 $-0.001\jmath$	1.941 $-0.040\jmath$	-0.062 $+0.000\jmath$	-0.841 $+0.009\jmath$
$M_{i,Pout}$	13.510 $-0.183\jmath$	-0.061 $+0.000\jmath$	17.196 $-0.240\jmath$	0.036 $-0.001\jmath$
$M_{i,Dout}$	-0.000 $+0.000\jmath$	-0.842 $+0.009\jmath$	0.035 $-0.001\jmath$	1.826 $-0.036\jmath$

Table A.25: Evaluated rotary array's inductance matrix at 1.5 MHz[1]

(µH)	$M_{Pin,j}$	$M_{Din,j}$	$M_{Pout,j}$	$M_{Dout,j}$
$M_{i,Pin}$	22.839 $-2.335\jmath$	-0.047 $-0.008\jmath$	17.774 $-1.996\jmath$	0.010 $-0.010\jmath$
$M_{i,Din}$	-0.049 $-0.011\jmath$	1.915 $-0.113\jmath$	-0.078 $-0.002\jmath$	-0.839 $+0.032\jmath$
$M_{i,Pout}$	17.689 $-1.944\jmath$	-0.080 $-0.005\jmath$	20.817 $-2.016\jmath$	0.047 $-0.014\jmath$
$M_{i,Dout}$	0.010 $-0.007\jmath$	-0.840 $+0.028\jmath$	0.046 $-0.013\jmath$	1.808 $-0.116\jmath$

[1]Notice that the real part is the actual inductance whereas the imaginary part is homogeneous to a resistance.

Table A.26: Evaluated rotary array's inductance matrix at 15 MHz[1]

(µH)	$M_{Pin,j}$	$M_{Din,j}$	$M_{Pout,j}$	$M_{Dout,j}$
$M_{i,Pin}$	-0.546 $+0.398\jmath$	0.001 $+0.002\jmath$	0.047 $-0.008\jmath$	0.002 $-0.003\jmath$
$M_{i,Din}$	0.001 $+0.002\jmath$	-0.782 $+0.662\jmath$	-0.004 $+0.001\jmath$	-0.354 $+0.023\jmath$
$M_{i,Pout}$	0.044 $-0.010\jmath$	-0.004 $+0.002\jmath$	-0.586 $+0.373\jmath$	0.009 $-0.003\jmath$
$M_{i,Dout}$	0.003 $-0.003\jmath$	-0.353 $+0.031\jmath$	0.010 $-0.001\jmath$	-0.868 $+0.662\jmath$

Appendix B

Numerical evaluation program

B.1 Usage

From a user point of view this code is very simple: it consists of a GNU Octave function which returns the inductance matrix for provided filamentary paths and their cross-section extrusion points. Below is the function's prototype:

```
output = inductance(inductor,...
         section, radius,...
         [resolution,plotInput])
```

- *inductor* is an **m*1 cell** of n-lines*3-columns matrices. Each line i of a matrix is interpreted as the 3D coordinates of the ith vertex of an induction path. Note that the circuit is automatically closed by a straight line during execution.
- *section* is an **m*1 or 1*1 cell** of n-lines*2-columns matrices. Each line i of a matrix is interpreted as the 2D coordinates of an integration point of the corresponding circuit's cross section.
- *area* is an **m*1 vector** of positive scalar which i^{th} value indicates the cross-section area of the i^{th} induction path.
- *resolution* is an optional positive scalar indicating the smallest desired length of the elements of the refined inputted paths. Default parameter 0 is interpreted as no refinement.

- *plotInput* is an optional boolean indicating whether or not to plot the inputted geometry. Default parameter is true.

- *output* is an n-lines*n-column matrix returning the mutual inductance M_{ij} between the ith and the jth induction path.

All inputted distances are considered meters. Permeability μ is considered constant and uniform, equal to $\mu = 4\pi\dot{1}0^{-7}$ H m^{-1}. Output result is expressed in Henri.

Example 1: We propose to calculate the mutual inductance between two coplanar toroidal circuits of mean-line radius $R_1 = 10\,\mathrm{m}$, $R_2 = 5\,\mathrm{m}$ and cross sectional radius $r_1 = 0.5\,\mathrm{m}$ and $r_2 = 0.25\,\mathrm{m}$. The total cross-section area is given by $A = 2 \times (\pi r^2)$. Mean lines are approximated by 361 points loops. Inductance can be calculated with the following set of commands:

```
r1 = 0.5;
r2 = 0.25;
x = cos([0:pi/180:2*pi]);
y = sin([0:pi/180:2*pi]);
R1 = [x(:).*10, y(:).*10,...
        zeros(361,1)];
R2 = [x(:).*5, y(:).*5, zeros(361,1)];
A = [r1^2; r2^2].*pi;
mutual = inductance({R1;R2},...
        {[0,0]}, A)
```

Above code generates the bellow Fig. B.1 and results in:

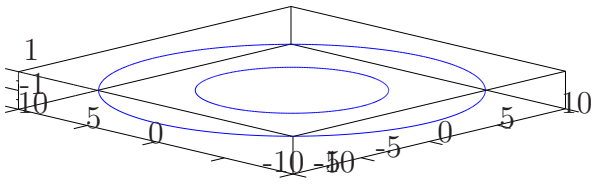

Figure B.1: Plot of the geometry of the Example 1

```
mutual =
3.7848e-005                5.4860e-006
5.4860e-006                1.3692e-005
```

where $3.7848e-005$ is an approximation of R_1 loop self inductance, $1.3692e-005$ is an approximation of R_2 loop self inductance and is an approximation of their mutual inductance.

Example 2: We propose to improve the self inductance approximation of R_1 loop by increasing the number of cross-section integration paths. We approximate the cross-section by a grid of regular triangles (Fig. B.2). Integration paths are the result of the extrusion of cross-section integration points (grid's faces center) along the mean-line R_1. We store 2D coordinates of those integration points in a 24lines*2columns text file called section.dat.

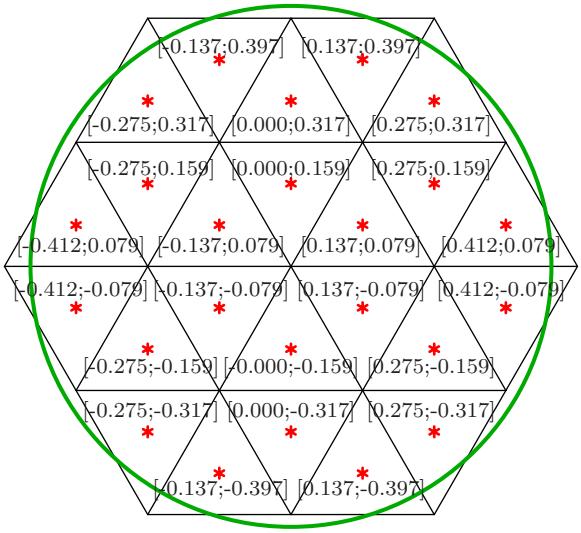

Figure B.2: Integrations point (red dot) are the face center of a regular grid of triangles (black lines) of total area equal to that of the ideal circular cross-section(green circle)

Inductance can be calculated with the following set of commands:

```
r1 = 0.5;
x = cos([0:pi/180:2*pi]);
y = sin([0:pi/180:2*pi]);
R1 = [x(:).*10, y(:).*10,...
        zeros(361,1)];
A = pi*r1^2;
fid = fopen('section.dat', 'r');
section = fscanf(fid, '%g %g',...
        [2, inf])';
fclose(fid);
```

```
self = inductance({R1}, {section}, A);
```

Above code generates the bellow Fig. B.3 and results in:

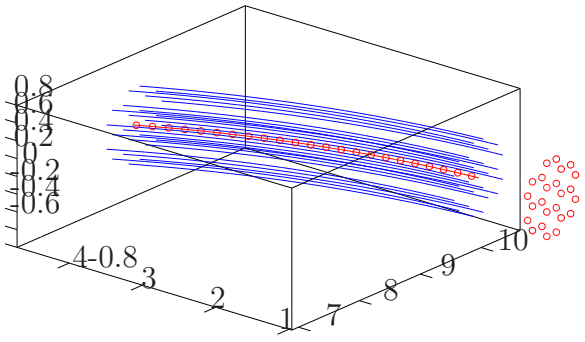

Figure B.3: Plot of a portion of the geometry of the Example 2. Red dots represents cross-section's integration points from which are extruded the blue integration paths along the red dotted mean line.

```
self =                4.1388e-005
```

Here the error compared to the theoretical value of 41.8 µH is about 1 %. We can try to improve the approximation by increasing the resolution of the paths by running those commands:

```
self = inductance({R1}, {section},...
        A, 0.05, 0);
```

which results in:

```
self =                4.1958e-005
```

It is important to note that those theoretical results might be quite different from reality due, for example, to the fact that the current is considered flowing in a conductor of magnetic permeability equal to μ_0. A better approach would consist for example in computing separately the internal and the external inductance as explained in [12].

B.2 Results

This code allow me to balance the self-inductance of each coil, progressively turning the design from Fig. B.4 to Fig. B.5 and finally to Fig. B.6.

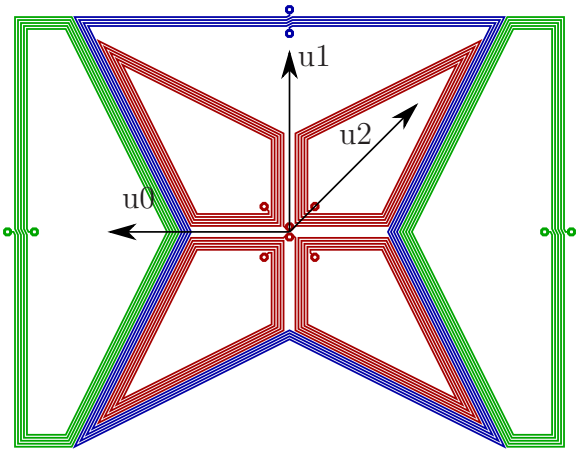

Figure B.4: Initial PCB antenna track design

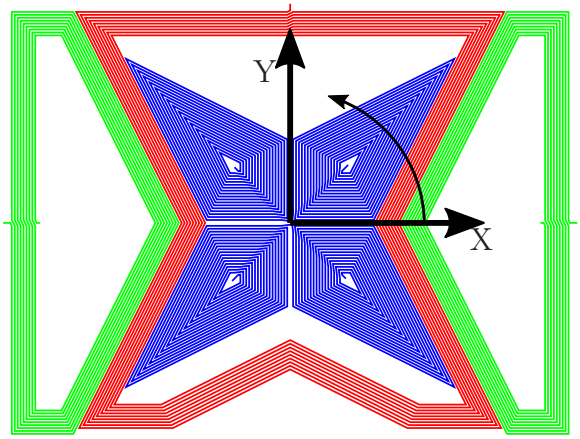

Figure B.5: First PCB antenna track design iteration

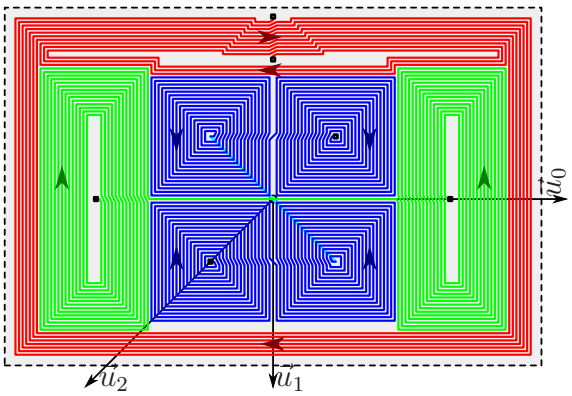

Figure B.6: Final track design

The final inductance matrix is given Fig. 2.6. Those results was obtained within a couple of hours of calculation, highlighting the fact that, given the pretty low level of complexity of the base problem, it was still quite a time consuming calculation.

References

[1] C. C. Ciang, J.-R. Lee, H.-J. Bang, *Structural health monitoring for a wind turbine system: a review of damage detection methods*, IOP Publishing — Measurement Sciences and Technologies, Vol 19, No. 12, October 2008

[2] A. Swartz, J. P. Lynch, S. Zerbst, B. Sweetman, R. Rolfes, *Structural monitoring of wind turbines using wireless sensor networks* , Smart Structures and Systems, Vol. 6, No. 3, pp 183-196, 2010

[3] A. Adamson, A. Berdugo, "Helicopter Slip Ring Replacement System," *International Telemetering Conference*, October 2010.

[4] K. M. Ebrahimi, A. Lewalski, A. Pezouvanis, B. Mason, "Piston Data Telemetry in Internal Combustion Engines," *American Journal of Sensor Technology*, Vol. 2, No. 1, pp 7-12, January 2014.

[5] G. F. Dorsey, D. S. Coleman, B. K. Witherspoon *High Speed Data Across Sliding Electrical Contacts* , IEEE 58th Holm Conference on Electrical Contacts (Holm), 2012

[6] LexInnova Technologies LLC, "Wireless Power Transmission: Patent Landscape Analysis." , 2015.

[7] R.J. Trew, "High-frequency solid-state electronic devices," *IEEE Trans. Electron Devices*, Vol. 52, No. 5, pp 638-649, May 2005.

[8] G. Ginis, J. M. Cioffi, "A multi-user precoding scheme achieving crosstalk cancellation with application to DSL systems," *IEEE, Conference Record of the Thirty-Fourth Asilomar Conference on Signals, Systems and Computers*, 2000.

[9] K. Sham, M. R. Ahmadi, S. B. G. Talbot, R. Harjani, "FEXT Crosstalk Cancellation for High-Speed Serial Link Design," *IEEE Custom Integrated Circuits Conference*, 2006.

[10] M. Bouchard, "Multichannel active noise control algorithms using inverse filters," *IEEE International Conference on Acoustics, Speech, and Signal Processing*, 2000.

[11] T. Oh, R. Harjani, "A 6-Gb/s MIMO Crosstalk Cancellation Scheme for High-Speed I/Os," *IEEE Journal of solid-state circuits*, Vol. 46, No. 8, pp 1843-1856, May 2005.

[12] T. Bieler, M. Perrottet, V. Nguyen and Y. Perriard, "Contactless Power and Information Transmission," *IEEE Trans. Industry Applications*, Vol. 38, No. 5, pp 1266-1272, September/October 2002.

[13] E. B. Rosa, "The self and mutual inductance of linear conductor," *Bul. of Bureau of Standard*, Vol. 4, No. 2, pp 301-344, 1908.

[14] G. L. Sugar, C. Vaidyanathan, Y. Tesfai, "System and method for antenna diversity using joint maximal ratio combining," *World International Property Organization*, Patent No. US 6 687 492 B1, Jun 2002.

[15] R. Stirling-Gallacher, "Multiple-input multiple output spatial multiplexing system with dynamic antenna beam combination selection capability," *World International Property Organization*, Patent No. US 8 369 436 B2, Feb. 2013.

[16] Christian Rathge and Daniel Kuschner, "High efficient inductive energy and data transmission system with special coil geometry," *13th European Conference on Power Electronics and Applications*, September 2009.

[17] V. J. Porter, "Magnetic recording heads utilizing symmetrical windings to avoid cross talk," *World International Property Organization*, Patent No. 3 287 713 , November 1966.

[18] R. C. Dorf, *The electrical engineering handbook, Second edition*, CRC press, September 1997.

[19] R. R. Harrison, "Designing Efficient Inductive Power Links for Implantable Devices," *IEEE International Symposium on Circuits and Systems*, May 2007.

[20] J. Hirai, T.-W. Kim, A. Kawamura, "Study on crosstalk in inductive transmission of power and information," *IEEE Trans. Industrial Electronics*, Vol. 46, No. 6, December 1999, pp 1174-1182.

[21] E. Kreyszig, *Advanced engineering Mathematics, tenth edition*, Wiley, August 2011.

[22] G. E. P. Box, J. S. Hunter, W. G. Hunter, *Statistics for Experimenters: Design, Innovation, and Discovery, 2nd Edition*, Wiley-Interscience, May 2005.

[23] J.-M. Chung, "Simultaneous inference of Jefimenko's and Maxwell equations from retardation," *Korean Physical Society*, Vol. 54, No. 6, December 2008.